



# Origin and implications of troilite-orthopyroxene intergrowths in the brecciated diogenite Northwest Africa 7183

Ai-Cheng Zhang<sup>a,b,\*</sup>, Yi-Fan Bu<sup>a</sup>, Run-Lian Pang<sup>a</sup>, Naoya Sakamoto<sup>c</sup>,  
Hisayoshi Yurimoto<sup>c,d</sup>, Li-Hui Chen<sup>a</sup>, Jian-Feng Gao<sup>e</sup>, De-Hong Du<sup>a</sup>,  
Xiao-Lei Wang<sup>a</sup>, Ru-Cheng Wang<sup>a</sup>

<sup>a</sup> State Key Laboratory for Mineral Deposits Research, School of Earth Sciences and Engineering, Nanjing University, Nanjing 210046, China

<sup>b</sup> Lunar and Planetary Science Institute, Nanjing University, Nanjing 210046, China

<sup>c</sup> Isotope Imaging Laboratory, Creative Research Institution Sousei, Hokkaido University, Sapporo 001-0021, Japan

<sup>d</sup> Department of Natural History Sciences, Hokkaido University, Sapporo 060-0810, Japan

<sup>e</sup> State Key Laboratory of Ore Deposit Geochemistry, Institute of Geochemistry, Chinese Academy of Sciences, Guiyang 550081, China

Received 27 October 2016; accepted in revised form 29 September 2017; Available online 7 October 2017

## Abstract

Troilite-orthopyroxene intergrowths are present as a common material in the brecciated diogenite Northwest Africa (NWA) 7183. In this study, we report on the petrographic, mineralogical, and rare earth element abundances of the troilite-orthopyroxene intergrowths to constrain their origin and assess their implications for the diverse petrogenesis of diogenites.

Two groups of troilite-orthopyroxene intergrowths with various grain sizes and mineral chemistry have been observed in NWA 7183. One group of intergrowths contains fine-grained (<5 μm) olivine and chromite as inclusions in orthopyroxene (10–20 μm in size). The other group, in which orthopyroxene is more fine-grained (<10 μm in size), is closely associated with coarse irregular olivine grains. The orthopyroxene grains in both groups of troilite-orthopyroxene intergrowths are depleted in Cr, Al, Ti, and Ca compared with diogenitic orthopyroxene. Based on the texture and mineral chemistry, we suggest that the two groups of troilite-orthopyroxene intergrowths formed via reactions between diogenitic olivine and S-rich vapors, probably at different temperatures. The fact that some of the intergrowths are included in diogenitic lithic clasts indicates that the formation of the host diogenite should postdate the formation of the majority of troilite-orthopyroxene intergrowths. This relationship further implies that not all of the diogenites are cumulates that directly crystallized from the Vestan magma ocean. Instead, they probably originated from partial melting and recrystallization of magma ocean cumulates. The replacement of olivine by troilite and orthopyroxene intergrowths can partly explain why the expected olivine-rich lithologies were not detected at the two south pole impact basins on Vesta.

© 2017 Elsevier Ltd. All rights reserved.

**Keywords:** Olivine; Troilite-orthopyroxene intergrowth; S-rich vapor; Northwest Africa 7183; Diogenite; Vesta

## 1. INTRODUCTION

The howardite-eucrite-diogenite (HED) meteorite clan represents a large group of achondrites ( $n = 1900$ ) composed of broadly basaltic (eucrite), orthopyroxene ± olivine cumulate (diogenite) and breccia (howardite) materials.

\* Corresponding author at: State Key Laboratory for Mineral Deposits Research, School of Earth Sciences and Engineering, Nanjing University, Nanjing 210046, China.

E-mail address: [aczhang@nju.edu.cn](mailto:aczhang@nju.edu.cn) (A.-C. Zhang).

They are considered to originate from Asteroid 4 Vesta based on the similarity of reflectance spectra between HED meteorites and the surface materials of Vesta (McCord et al., 1970; Mittlefehldt et al., 1998; McSween et al., 2011; Mittlefehldt, 2015). The HED meteorites are important samples for constraining the differentiation and evolution of this unique proto-planet (Russell et al., 2012) and subsequent processing events (Treiman et al., 2004; Barrat et al., 2011; Day et al., 2012; Zhang et al., 2013; Warren et al., 2014; Miyahara et al., 2014; Pang et al., 2016). The eucritic components are composed mainly of pyroxene and plagioclase. Based on textural differences, they are subdivided into cumulate eucrites and basaltic eucrites. It is widely accepted that eucrites are samples from the upper crust of the eucrite parent body, regardless of their detailed formation models (Mittlefehldt, 1994; Mittlefehldt et al., 2012; McSween et al., 2011; Mandler and Elkins-Tanton, 2013; Mittlefehldt, 2015). Diogenitic components are composed predominantly of orthopyroxene and olivine with minor diopside/augite, chromite, and plagioclase. They can be subdivided into orthopyroxenitic, harzburgitic, and dunitic diogenites based on the relative abundances of orthopyroxene and olivine (Mittlefehldt, 2015). The petrogenesis of diogenites is still an issue of controversy. Some investigators have proposed that diogenites could have formed as cumulates from a magma ocean (Richter and Drake, 1997; Ruzicka et al., 1997; McSween et al., 2011; Mandler and Elkins-Tanton, 2013; Mittlefehldt, 2015). On the other hand, other investigators have argued that at least some diogenites might have a more complex petrogenesis (Barrat et al., 2008, 2010; Yamaguchi et al., 2011; Barrat and Yamaguchi, 2014). For example, based on trace element geochemistry (e.g., Eu anomalies and Dy/Yb ratios) of orthopyroxene in certain diogenites, Barrat et al. (2008, 2010) suggested that some diogenites might have formed by the remelting of magma ocean cumulates and that others were contaminated with melts derived by partial melting of the eucritic crust. Based on the presence of chemically zoned orthopyroxene, Yamaguchi et al. (2011) argued that diogenites are not the products of the crystallization of the Vestan magma ocean. Instead, they proposed that diogenites are cumulates associated with a later stage of magmatism on Vesta.

Although the origin of diogenites remains an issue of debate, the earliest differentiation and evolution of Vesta is generally well understood based on magma-ocean models. Olivine-rich diogenites were expected to be present in the mantle of Vesta (Richter and Drake, 1997; Ruzicka et al., 1997; Mandler and Elkins-Tanton, 2013). However, no olivine-rich diogenites were detected at the most probable locations (deep south pole basins) on the surface of Vesta by the Visible and Infrared Mapping Spectrometer on board the NASA Dawn spacecraft (De Sanctis et al., 2012; Ammannito et al., 2013a, 2013b; McSween et al., 2013; Palomba et al., 2015; Le Corre et al., 2015; Nathues et al., 2015). Several scenarios have been proposed to explain the non-detection of olivine-rich lithologies at the two deep south pole basins on Vesta. They include the following: (1) the Dawn Visible and Infrared Mapping Spectrometer cannot distinguish harzburgites from

orthopyroxenites due to the low initial olivine abundance (10–30%; Beck et al., 2013; Nathues et al., 2015); (2) olivine dilution occurs through impact gardening (Beck et al., 2013); (3) the Vestan crust could be thicker than previously thought (Nathues et al., 2015; Turrini et al., 2016); and (4) the magma-ocean models cannot be straightforwardly applied to Vesta (Palomba et al., 2015). However, whether and how olivine-rich lithologies on Vesta have been modified by secondary processes remains unknown.

Troilite usually occurs as an accessory mineral in HED meteorites (Day et al., 2012; Mittlefehldt, 2015). However, it has been observed as a major constituent mineral within a few lithic clasts and mineral fragments in brecciated HED meteorites (Hewins, 1981; Patzer and McSween, 2012; Zhang et al., 2013; Eckley et al., 2016). One occurrence of troilite as a major phase is in a few fragments of vermicular intergrowth with orthopyroxene in howardites (Patzer and McSween, 2012) and two brecciated diogenites (Garland, Hewins, 1981; NWA 10451, Eckley et al., 2016). Hewins (1981) suggested that the orthopyroxene associated with troilite formed through reaction of olivine with liquid. Patzer and McSween (2012) and Eckley et al. (2016) proposed that the troilite-orthopyroxene intergrowth might have developed via impact-induced localized melting of diogenitic orthopyroxene in the presence of troilite. The other occurrence of troilite as a major phase is fine-grained troilite closely associated with high-Ca pyroxene and silica in the brecciated eucrite NWA 2339 (Zhang et al., 2013). Zhang et al. (2013) suggested that such a troilite-rich mineral assemblage might have formed via an interaction between Fe-rich pyroxene and S-rich vapors at the Vestan surface.

Recently, we observed that troilite-orthopyroxene intergrowths are commonly present in the brecciated diogenite meteorite Northwest Africa (NWA) 7183. In some lithic clasts of NWA 7183, the troilite-orthopyroxene intergrowths show a close association with typical diogenitic orthopyroxene, providing an important clue to constrain the petrogenesis of diogenite. In this study, we report detailed petrography, mineral chemistry, and rare earth element (REE) abundances of the troilite-orthopyroxene intergrowths in NWA 7183 and discuss their origins and implications for the diverse petrogenesis of diogenites. We also discuss their potential implications for the non-detection of olivine-rich lithologies at the two large south pole basins on Vesta.

## 2. SAMPLE AND ANALYTICAL METHODS

The meteorite NWA 7183 is a polymict brecciated diogenite that was found in Morocco (Ruzicka et al., 2014). In this study, we analyzed three thin sections of NWA 7183. Petrographic textures of lithic clasts in NWA 7183 were mainly observed with a JEOL 7000F Field Emission Gun Scanning Electron Microscope (FEG-SEM) at Hokkaido University, Japan. The FEG-SEM instrument was operated with an accelerating voltage of 15 kV and a beam current of 2 nA. Back-scattered electron (BSE) images were used to determine the modal abundances of major constituent minerals in the troilite-orthopyroxene intergrowths

by obtaining the pixel numbers corresponding to troilite, orthopyroxene, olivine, and the whole intergrowth. The modal abundance was calculated based on the ratio between the pixel numbers for a certain mineral and for the whole intergrowth. X-ray elemental mapping was performed on several troilite-orthopyroxene intergrowths using an energy dispersive X-ray spectrometer (EDS, Oxford X-Max 150) installed on this FEG-SEM instrument. A beam current of 10 nA accelerated at 15 kV was used for the X-ray elemental mapping. Crystallographic orientation mapping of troilite and orthopyroxene was obtained using an Electron Backscatter Diffraction (EBSD) detector equipped on a JEOL 6490 SEM at Nanjing University and controlled by the Aztec Software. The accelerating voltage was 20 kV.

The mineral chemistry of silicate, oxide, and sulfide minerals was determined with a JEOL 8100 electron probe micro-analyzer (EPMA) using wavelength dispersive spectrometers at Nanjing University, China. A focused beam current ( $\sim 1 \mu\text{m}$  in diameter) of 20 nA, accelerated at 15 kV, was used for the silicate and oxide minerals. Sulfide minerals in this study were analyzed with an accelerating voltage of 20 kV and a beam current of 20 nA. A few natural and synthetic materials were used as standards for calibration. All data were reduced with the ZAF correction procedure. Typical detection limits for most elements in silicate minerals were  $\sim 0.02 \text{ wt}\%$ .

The REE compositions of pyroxenes in NWA 7183 were determined with the Cameca IMS-6f instrument at Hokkaido University. The procedure has been described elsewhere (Yurimoto et al., 1989; Wang and Yurimoto, 1993; Zhang et al., 2014). The primary beam was mass filtered  $^{16}\text{O}^-$  of  $-14.5 \text{ keV}$  and irradiated on the sample surface to a diameter of  $\sim 25 \mu\text{m}$ . The primary beam current was 10–15 nA. Kinetic energy filtering was used to reduce interferences from molecular ions by offsetting the sample acceleration voltage ( $-60 \text{ eV}$ ). The energy bandwidth was 20 eV. The entrance and exit slits and the field aperture were fully open with a mass resolving power of  $\sim 500$ . Positive secondary ion intensities of rare earth elements were counted for 10 s with an electron multiplier detector in magnetic peak-jumping mode, while the secondary ion intensity of  $^{30}\text{Si}$  was counted for 1 s with the same electron multiplier detector. Each analysis included 15 cycles. The relative sensitivity factors between secondary ion intensity and concentration for each REE (relative to Si) were determined using the Takashima augite, whose REE contents have been well determined by instrumental neutron activation analysis (Onuma et al., 1968).

To constrain the potential source of sulfur in the troilite-orthopyroxene intergrowths from NWA 7183, we measured the concentrations of siderophile and chalcophile elements including Os, Ir, Ru, Rh, Pd, Pt, Au, As, Se, Te, Sb, and Bi in troilite. These elements were measured using the Agilent 7700x mass spectrometer coupled to a Newwave NWR 213-nm laser ablation system at the Institute of Geochemistry, Chinese Academy of Sciences, Guiyang, China. The troilite grains were analyzed using individual spots with a 20- $\mu\text{m}$  diameter. Each analysis consisted of  $\sim 70 \text{ s}$  of data collection. Backgrounds on the ICP-MS sample gas were

collected for approximately 20 s followed by approximately 50 s of laser ablation of the sample. Three major elements and twelve trace elements were analyzed using following isotopes  $^{29}\text{Si}$ ,  $^{34}\text{S}$ ,  $^{57}\text{Fe}$ ,  $^{75}\text{As}$ ,  $^{77}\text{Se}$ ,  $^{101}\text{Ru}$ ,  $^{103}\text{Rh}$ ,  $^{104}\text{Pd}$ ,  $^{105}\text{Pd}$ ,  $^{121}\text{Sb}$ ,  $^{125}\text{Te}$ ,  $^{189}\text{Os}$ ,  $^{193}\text{Ir}$ ,  $^{195}\text{Pt}$ ,  $^{197}\text{Au}$ , and  $^{209}\text{Bi}$ .  $^{57}\text{Fe}$  was measured as an internal standard, and  $^{29}\text{Si}$  was measured to monitor the contribution of silicate minerals adjacent to troilite. PGE-A, a synthetic NiS bead doped with platinum group elements, Au, and a few chalcophile elements, was used as an external standard for most of the above trace elements. Mass-1 was used as an external standard for Se. The silicate glass GSE-1G, a synthetic basaltic glass, was used as another external standard to determine the relative sensitivity factors of Si and Fe. The  $^{57}\text{Fe}$  counts contributed by orthopyroxene were subtracted from those for the troilite-orthopyroxene mixture, assuming that the orthopyroxene had relative sensitivity factors of Si and Fe identical to those in the GSE-1G glass due to similar matrix effects. Then,  $^{57}\text{Fe}$  was used as an internal standard to calibrate the concentrations of siderophile and chalcophile elements. The standards were measured before and after the analyses on the troilite in NWA 7183. Because siderophile and chalcophile elements have very high affinities for sulfide relative to silicate or oxide minerals (Day et al., 2016), we assumed that the measured signals for the siderophile and chalcophile elements were mainly from troilite rather than from surrounding orthopyroxene.

### 3. RESULTS

#### 3.1. Petrography and mineralogy

The meteorite NWA 7183 shows a texture typical of brecciated samples (Fig. 1), consisting mainly of angular mineral fragments and minor amounts of lithic clasts (60–1300  $\mu\text{m}$  in size). The most common mineral fragments are pyroxene and plagioclase. Pyroxene fragments are generally larger in size than plagioclase fragments and can be as large as  $\sim 2 \times 7 \text{ mm}$  (Fig. 1). Many of the orthopyroxene fragments in NWA 7183 have bright rims ( $\sim 20 \mu\text{m}$  in width) along grain boundaries or fractures (Fig. 2). A few diagenetic clasts contain rounded olivine grains (10–200  $\mu\text{m}$  in size) as inclusions within orthopyroxene. In addition to the abundant orthopyroxene fragments, some of the pyroxene fragments in NWA 7183 are pigeonite and contain thin exsolution augite lamellae ( $< 3 \mu\text{m}$  in width). A few pigeonite fragments are partially replaced by a fine-grained mineral assemblage of augite, silica, and troilite (Fig. 3), resembling those described in the brecciated eucrite NWA 2339 (Zhang et al., 2013). Individual fragments of olivine, chromite, and ilmenite are also observed in NWA 7183 but are much less abundant than pyroxene and plagioclase. A few eucritic lithic clasts with subophitic or cumulate textures are observed in NWA 7183. A few crystalline impact breccias and possible chondritic materials (e.g., Fe-Ni metal grains) are also present in NWA 7183. Some Fe-Ni metal (1.65–1.72 wt% Ni) and troilite grains have been partially weathered. However, no mineralogical evidence of terrestrial weathering is observed in the pyroxene and plagioclase of NWA 7183.

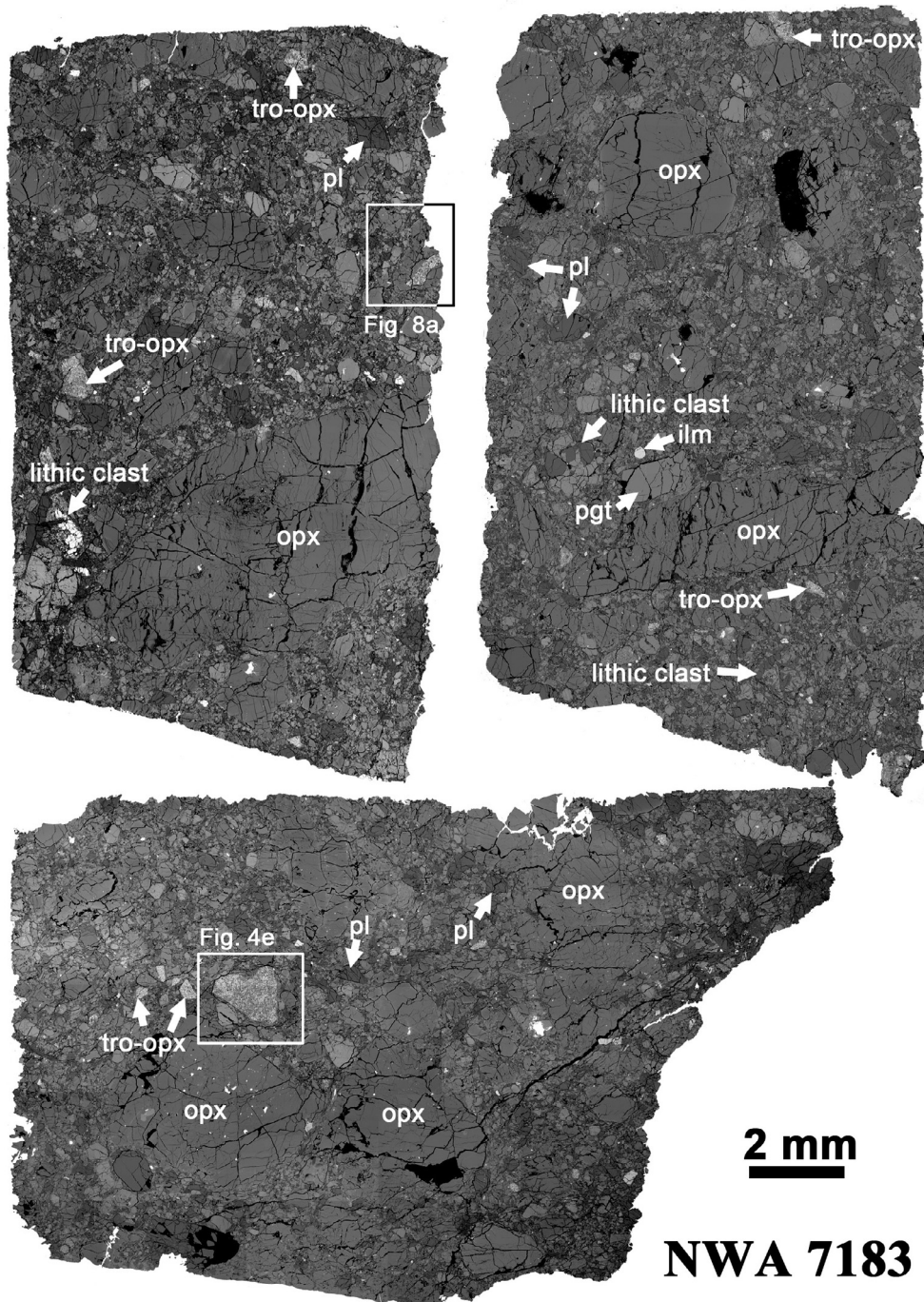


Fig. 1. Mosaic backscattered electron images of NWA 7183 polymict diogenite. The rectangular outlines show the positions of the two clasts (Figs. 4e and 8a) containing two sets of troilite-orthopyroxene intergrowth with different grain sizes. Opx: orthopyroxene; pgt: pigeonite; ilm: ilmenite; pl: plagioclase; tro-opx: troilite-orthopyroxene intergrowth.

More than fifty clasts of the troilite-orthopyroxene intergrowths are observed in this study, and representative textures are shown in Fig. 4. They usually exhibit irregular outlines and vary in size from  $\sim 100$  to  $\sim 1400$   $\mu\text{m}$ . Most of them consist predominantly of orthopyroxene and troilite, with minor amounts of olivine and chromite. It is noteworthy that Fe-Ni metal is present in a few intergrowths of troilite-orthopyroxene (e.g., Fig. 4c and e), although it is

not observed in most of the intergrowths in NWA 7183. The orthopyroxene (abbreviated as Opx-I hereafter) and troilite have similar grain sizes (10–20  $\mu\text{m}$ ), with anhedral troilite filling the interstitial regions between orthopyroxene grains. In some cases, troilite grains are interconnected (Fig. 4a). Optical observations show that the orthopyroxene grains in some of the intergrowths display optical continuity. However, some intergrowths contain multiple

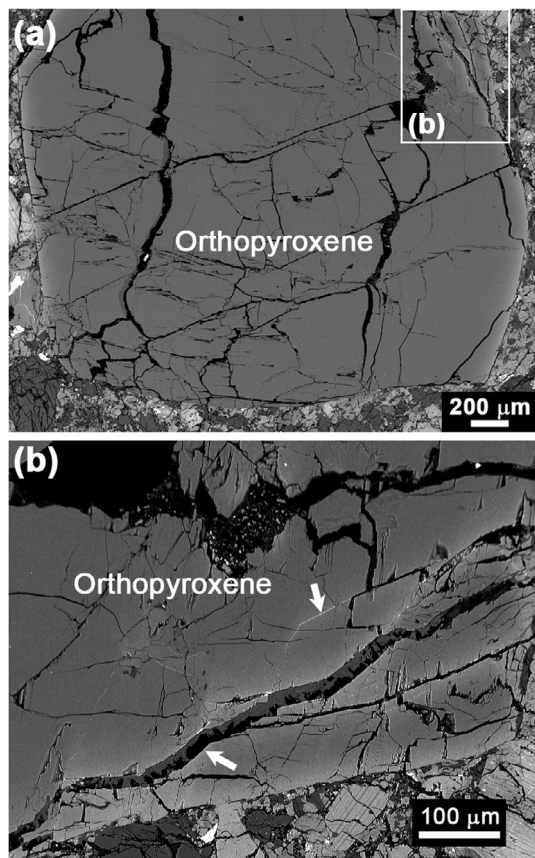


Fig. 2. Backscattered electron image (a) of a coarse-grained diagenetic orthopyroxene grain with a thin, bright zone along grain rim and fractures. (b) Close-up image of the rectangle region indicated in (a). White arrows indicate the locations of fractures with bright zones.

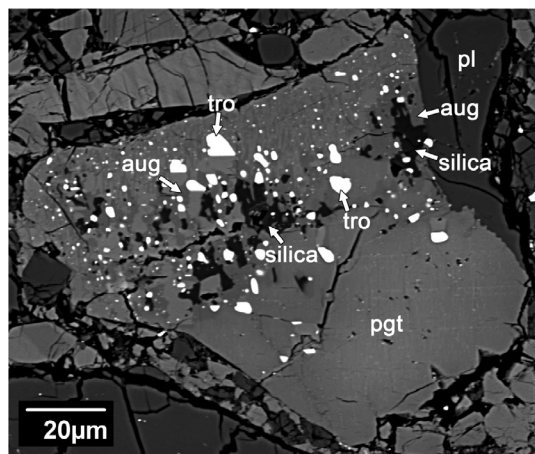


Fig. 3. Backscattered electron image of a lithic clast in which Fe-pigeonite has been partially metasomatized to augite, silica, and troilite.

discontinuous domains, but within each domain, the orthopyroxene also displays optical continuity (Fig. 5). The EBSD Euler mapping result reveals more complex

crystallographic orientations of both orthopyroxene and troilite (Fig. 6). For example, the orthopyroxene in the upper-left region in Fig. 6c displays crystallographic continuity; however, troilite therein displays varying orientations. The apparent modal abundance of troilite varies from 8 to 21 vol% in different intergrowths (Fig. 7). In the troilite-orthopyroxene intergrowths, olivine and chromite, if present, mainly occur as very fine-grained (<5 μm) mineral inclusions in orthopyroxene (Fig. 4b–d). In some troilite-orthopyroxene intergrowths, however, olivine has a high modal abundance up to ~12 vol%, and its grain size is up to 150 μm (Fig. 4e). Almost all of the coarse olivine grains are irregular in shape (Fig. 4e and f). In the troilite-orthopyroxene intergrowths with coarse olivine grains, some regions are composed of more fine-grained intergrowths (<10 μm in size) of troilite and orthopyroxene (abbreviated as Opx-II hereafter). The more fine-grained (<10 μm) troilite-orthopyroxene intergrowths have a close association with the coarse olivine grains (Fig. 4f).

Although the troilite-orthopyroxene intergrowths in NWA 7183 occur mainly as individual lithic clasts (Fig. 4), some of them are closely associated with typical diagenetic clasts (Figs. 8 and 9). The fragments of the troilite-orthopyroxene intergrowths are included or embayed in typical diagenite clasts (Fig. 8). Both of the fragments of troilite-orthopyroxene intergrowths shown in Fig. 8 have smooth and rounded boundaries with surrounding diagenitic orthopyroxene grains. Shown in Fig. 8a is a diagenite clast approximately 1.5 mm in size and containing an inclusion of troilite-orthopyroxene intergrowth. This lithic clast consists dominantly of coarse-grained orthopyroxene crystals, with minor amounts of plagioclase and chromite located at the grain boundaries between orthopyroxene crystals (Fig. 8a). The coarse orthopyroxene grains in this clast also show bright rims (~20 μm in width) along grain boundaries (Fig. 8a and b). In this diagenite clast, the troilite-orthopyroxene intergrowth has a high modal abundance of olivine (~8 vol%). Some of the olivine grains are also coarse and irregular in shape. Texturally, the troilite-orthopyroxene intergrowth is similar to those present as individual fragments with coarse-grained olivine (e.g., Fig. 4e and f). Both groups of troilite-orthopyroxene intergrowths are present, and the Opx-II and associated troilite also appear replacing olivine grains (Fig. 8b and c). In the lithic clast shown in Fig. 9a, the troilite-orthopyroxene intergrowth, which contains a small irregular olivine grain, partly encloses a coarse orthopyroxene grain. The X-ray mapping of Ca indicates a sharp grain boundary between the intergrowth and the enclosed orthopyroxene grain (Fig. 9b). The orthopyroxene grain enclosed by the troilite-orthopyroxene intergrowth also has a bright rim (~20 μm in width) in the BSE image (Fig. 9a), consistent with the enrichment of Fe (Fig. 9c).

### 3.2. Mineral chemistry

The EPMA results reveal that all plagioclase grains observed in NWA 7183 are anorthitic in composition ( $An_{76.2}$  to  $An_{94.5}$ ), which is in the compositional range for plagioclase in HED meteorites (Mittlefehldt, 2015). The

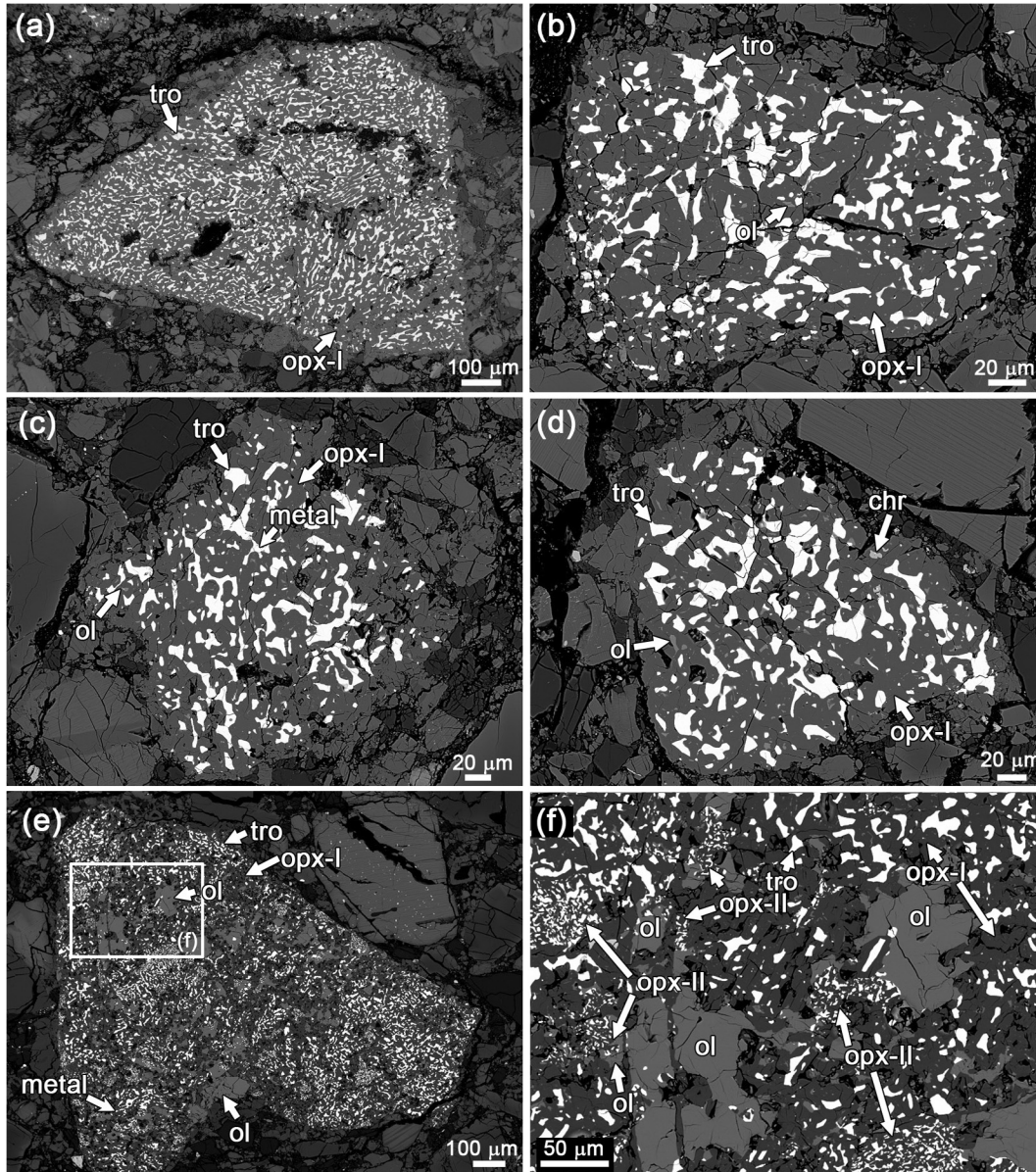


Fig. 4. Backscattered electron images of troilite-orthopyroxene intergrowth in NWA 7183. (a) The troilite grains connect with each other, with a wetting texture. (b–d) Fragments of troilite-orthopyroxene intergrowth that contain olivine and chromite as small inclusions. Note that a Fe-Ni metal grain of 6  $\mu\text{m}$  in size is present in (c). (e) A fragment of olivine-bearing troilite-orthopyroxene intergrowth. This fragment contains two groups of troilite-orthopyroxene intergrowth with various grain sizes. Note that a Fe-Ni metal grain is also present in this intergrowth. (f) Close-up image of the rectangle region indicated in (e) showing the association between finer-grained troilite-orthopyroxene intergrowth and olivine.

majority of pyroxene grains in NWA 7183 are orthopyroxene, and their Fe-Mn compositions are consistent with the trend for HED pyroxenes (Fig. 10). Generally, our petrographic and mineralogical observations support the idea that NWA 7183 is a brecciated diogenite meteorite (Ruzicka et al., 2014).

Chemically, the pyroxenes in NWA 7183 have large variations in composition, ranging from orthopyroxene through pigeonite to augite (Fig. 11). Representative compositions are given in Table 1. Most grains of the diogenitic orthopyroxene in NWA 7183 have a limited

compositional range ( $\text{En}_{68.8-75.9}\text{Fs}_{22.1-28.4}\text{Wo}_{2.1-4.1}$ ) with  $\text{Mg\#}$  ( $=100 \cdot \text{Mg}/(\text{Mg} + \text{Fe})$  in mole) values of 71.0–77.6, consistent with those of typical diogenitic orthopyroxene in previous studies (see Mittlefehldt, 2015; Fig. 11 and Table 1). However, the bright rims of some diogenitic orthopyroxene grains are Fe-rich ( $\text{En}_{55.7-64.0}\text{Fs}_{33.5-42.5}\text{Wo}_{1.7-4.1}$ ) with  $\text{Mg\#}$  values of 56.7–65.7 (Table 1). The contents of  $\text{TiO}_2$  (0.02–0.74 wt%),  $\text{Al}_2\text{O}_3$  (0.68–1.60 wt%), and  $\text{Cr}_2\text{O}_3$  (0.32–0.94 wt%) in the diogenitic orthopyroxene from NWA 7183 are generally consistent with those reported in the literature (Mittlefehldt, 2015; Fig. 12).

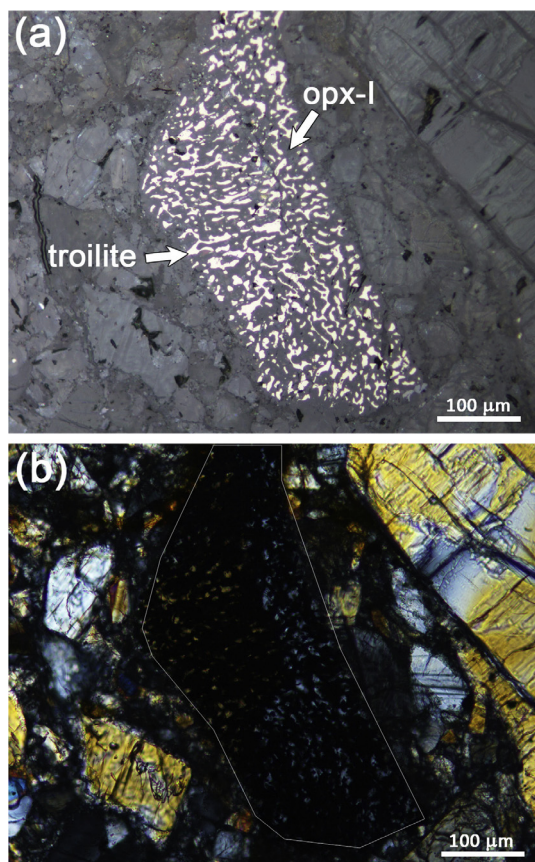


Fig. 5. Reflected light (a) and cross-polarized transmission light (b) microscopic images of an orthopyroxene-troilite intergrowth in NWA 7183. Note the optical discontinuity of orthopyroxene in the outlined region in (b).

Eucritic pyroxenes in NWA 7183 have a large compositional range and are generally more Fe-rich than diagenitic orthopyroxenes (Fig. 11 and Table 1). The orthopyroxene in the troilite-orthopyroxene intergrowth is also more Fe-rich compared with the majority of diagenitic orthopyroxene but is comparable to the Fe-rich rims of diagenitic orthopyroxene (Table 1). The Opx-I in troilite-orthopyroxene intergrowths has compositions of  $\text{En}_{54.9-62.6}\text{Fs}_{37.0-43.9}\text{Wo}_{0.9-1.5}$  with Mg# values of 55.6–62.7. Their Al and Cr concentrations are much lower than those in diagenitic orthopyroxene and Ti and Ca concentrations slightly lower than those in diagenitic orthopyroxene from NWA 7183 (Fig. 12 and Table 1). The Opx-II in the intergrowths contains even lower Fs and Wo contents ( $\text{En}_{61.0-64.3}\text{Fs}_{35.1-38.4}\text{Wo}_{0.5-0.7}$ ; Fig. 11 and Table 1) with Mg# values of 61.4–64.6. Meanwhile, the Al, Cr, Ti, and Ca concentrations in Opx-II are slightly lower than those in Opx-I (Fig. 12 and Table 1).

The chemical compositions of olivine in a few lithic clasts were also determined in this study (Table 2). Rounded olivine grains have different chemical compositions in two different diagenitic clasts. In one diagenitic clast, the olivine grains, which are 10–20 µm away from the Fe-rich rim of orthopyroxene, have Mg# values of 69.7–69.9. These Mg# values are within the compositional

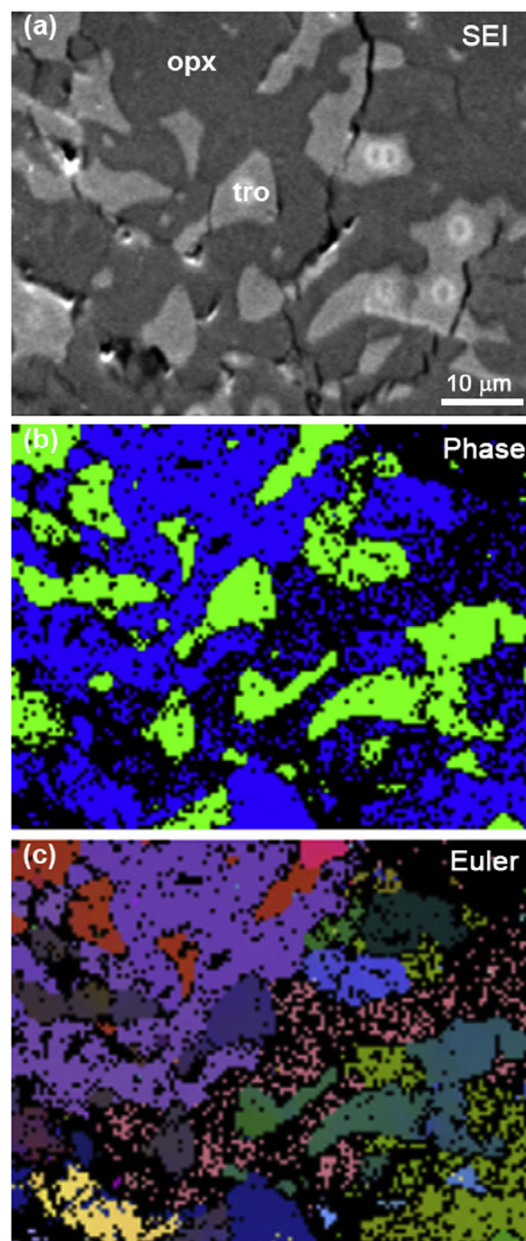


Fig. 6. Secondary electron image (a), Phase map (b), and EBSD Euler map (c) of a typical area of troilite-orthopyroxene intergrowth in NWA 7183. Note that both orthopyroxene and troilite grains have various crystallographic orientations, with different colors in the Euler map. Opx: orthopyroxene; tro: troilite. (For interpretation of the references to colour in this figure legend, the reader is referred to the web version of this article.)

range for diagenitic olivine described in previous studies (Mittlefehldt, 2015; Fig. 13). However, in another diagenitic clast, an olivine grain that is located at the bright (Fe-rich) margin of orthopyroxene has an Mg# value of 54.0, which is out of the range in Mittlefehldt (2015). The  $\text{Cr}_2\text{O}_3$  contents of olivine within both diagenitic clasts are 0.08–0.10 wt%, and the  $\text{Al}_2\text{O}_3$  and  $\text{TiO}_2$  contents are below detection limits (Table 2). Compared with the diagenitic olivine in NWA 7183, all the olivine grains in troilite-

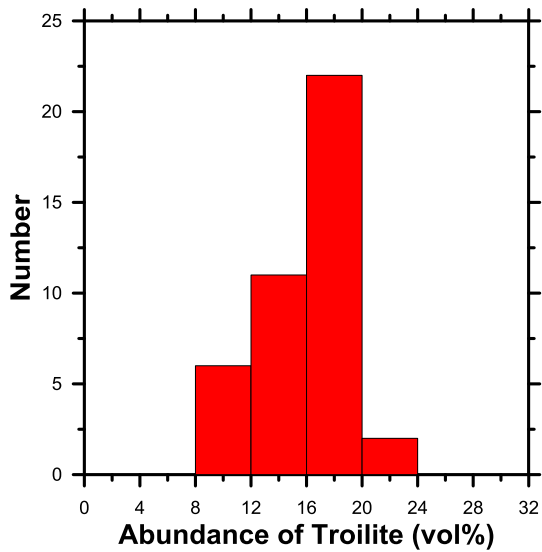


Fig. 7. Distributions of troilite modal abundance (vol%) in the troilite-orthopyroxene intergrowth from NWA 7183.

orthopyroxene intergrowths are Fe-rich ( $Mg\# = 39.4\text{--}53.3$ ; Fig. 13). The coarse-grained olivine and the tiny grains within individual lithic clasts with the troilite-

orthopyroxene intergrowths have almost identical compositions. The  $Cr_2O_3$  contents of olivine in the troilite-orthopyroxene intergrowths vary from below detection limit to 0.04 wt%, and the  $Al_2O_3$  and  $TiO_2$  contents are below detection limits (Table 2). Nickel is not detected in olivine with a detection limit of  $\sim 0.02$  wt%. The chromite grains in diagenetic clasts have compositions of  $Chr_{64.7\text{--}67.6}Spl_{28.6\text{--}32.1}Usp_{2.5\text{--}3.7}$  with low  $Mg\#$  values of 5.2–6.6. The chromite grains in troilite-orthopyroxene intergrowths have similar compositions ( $Chr_{70.0\text{--}72.7}Spl_{21.2\text{--}25.0}Usp_{5.0\text{--}6.2}$ ,  $Mg\# = 5.1\text{--}5.5$ ; Table 2). It is noteworthy that the  $Mg\#$  values of chromites from both diagenetic clasts and the troilite-orthopyroxene intergrowths are lower than those (7.7–31.7) for chromite in typical diagenetic clasts compiled by Mittlefehldt (2015). Troilite contains minor Co (0.09–0.12 wt%), and no Ni is detected. The molar values for  $S/(Fe + Co)$  are 0.981–1.024 (Table 3). Fe-Ni metal in a few troilite-orthopyroxene intergrowths contains 1.6–1.7 wt% Ni, comparable to the relatively coarse-grained Fe-Ni metal in NWA 7183 that is not associated with the troilite-orthopyroxene intergrowths.

### 3.3. Rare-earth elements of pyroxene

We measured rare earth element concentrations in a few pyroxene grains within lithic clasts and mineral fragments

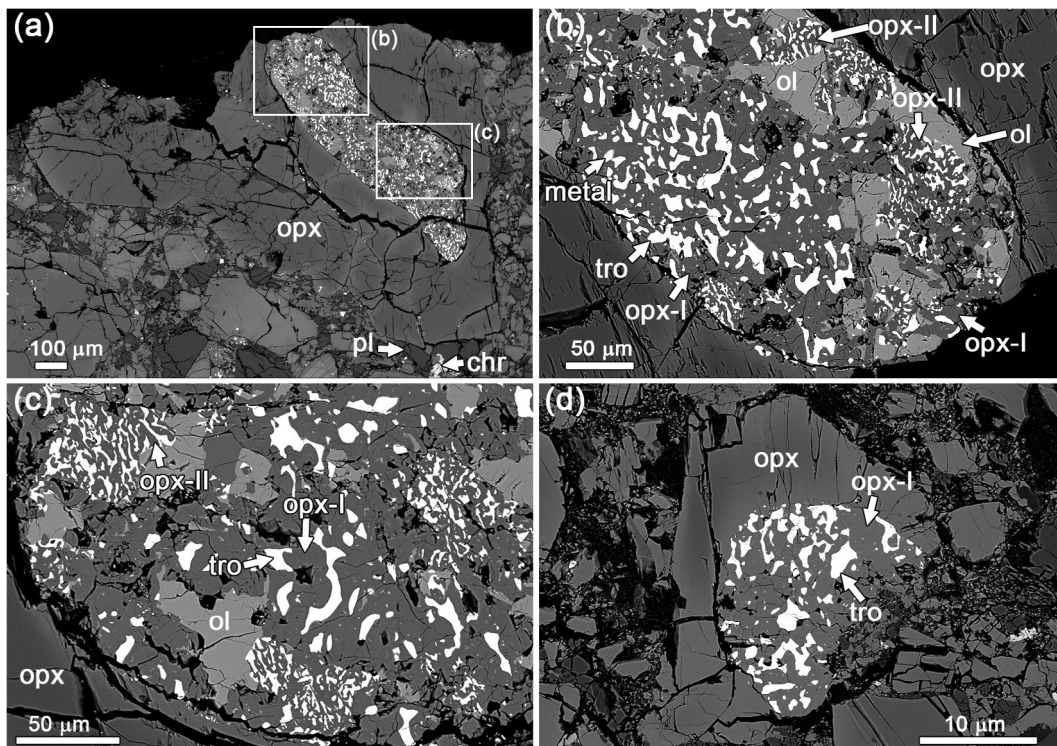


Fig. 8. Backscattered electron images of the troilite-orthopyroxene intergrowth included in diagenetic orthopyroxene. (a) A diagenetic clast contains a fragment of olivine-bearing troilite-orthopyroxene intergrowth. The diagenetic orthopyroxene grains are associated with plagioclase and chromite (lower part of the clast). The fragment has a smooth boundary with surrounding diagenetic orthopyroxene. (b and c) Close-up images of the rectangle regions indicated in (a). Note that a FeNi metal grain is present in (b). There are two groups of troilite-orthopyroxene intergrowth. The finer group of troilite-orthopyroxene intergrowth shows a close association with irregular olivine grains. (d) A small diagenetic orthopyroxene containing troilite-orthopyroxene intergrowth. The intergrowth also has a rounded shape. Opx: orthopyroxene; pl: plagioclase; chr: chromite; ol: olivine; tro: troilite.

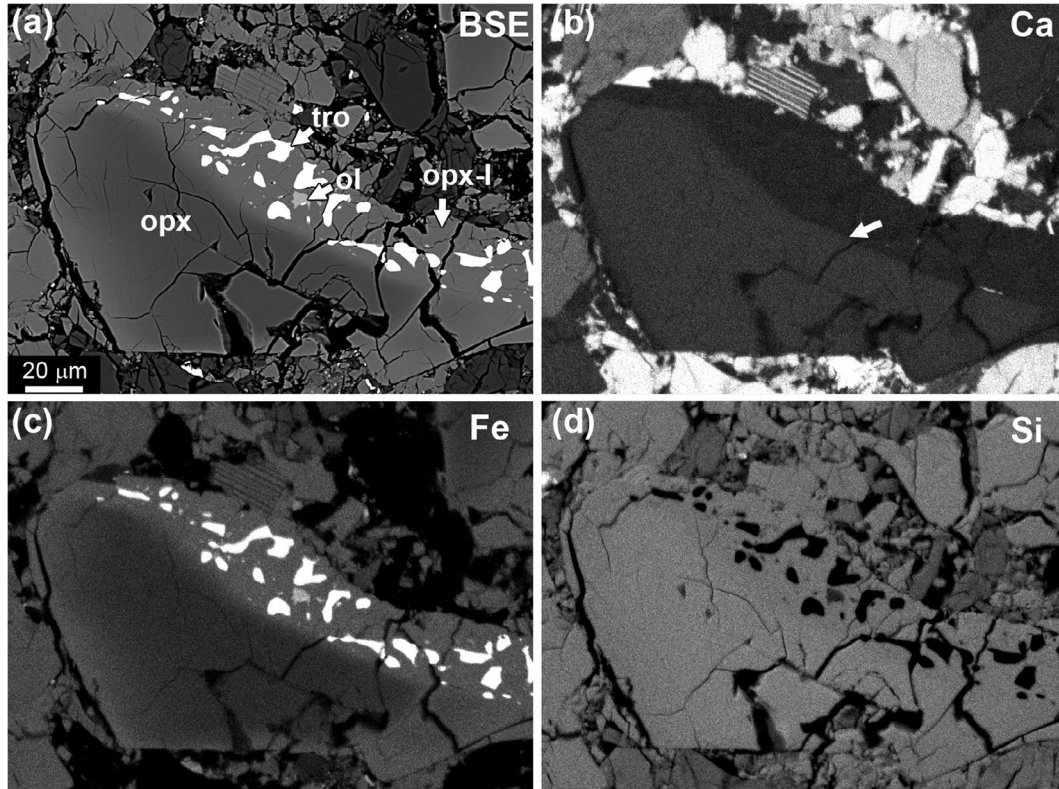


Fig. 9. Backscattered electron image (a) and X-ray mapping results (b–d) of a clast containing the troilite-orthopyroxene intergrowth. Note that the troilite-orthopyroxene intergrowth partly encloses a fragment of diagenetic orthopyroxene. An irregular olivine grain is included in orthopyroxene. The white arrow in (b) indicates the sharp boundary between diagenetic orthopyroxene and the troilite-orthopyroxene intergrowth. Tro: troilite; ol: olivine; opx: orthopyroxene; opx-I: orthopyroxene in the troilite-orthopyroxene intergrowth.

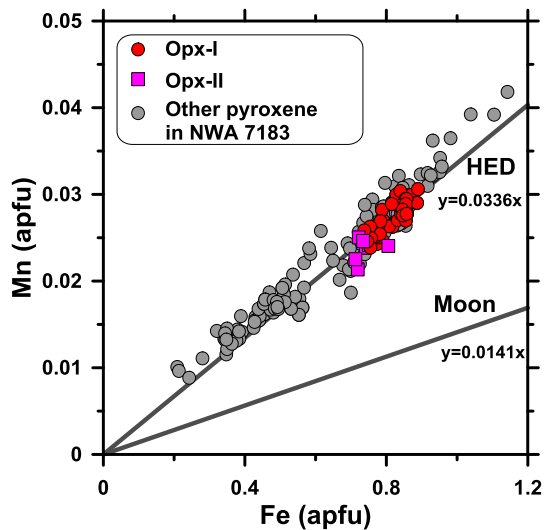


Fig. 10. Fe-Mn compositions of pyroxene grains in NWA 7183. The trends for pyroxene in HED meteorites and lunar samples are from Papike et al. (2003).

using the SIMS technique (Table 4). One large ( $\sim 2 \times 7$  mm) diagenetic orthopyroxene grain ( $\text{En}_{73.1}\text{Fs}_{24.1}\text{Wo}_{2.8}$ ) has the lowest REE concentrations in this study (blue patterns in Fig. 14a). This diagenetic orthopyroxene grain is enriched

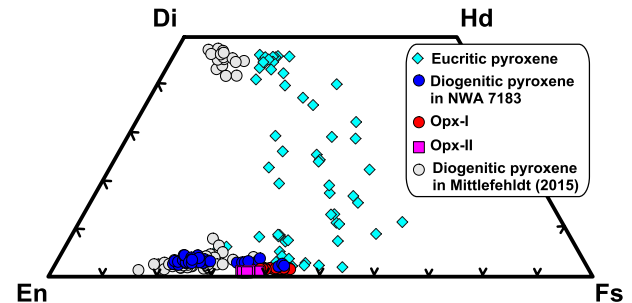


Fig. 11. Chemical compositions of major elements of pyroxenes (symbols in color) in NWA 7183, in comparison with diagenetic pyroxene in the literature (Mittlefehldt, 2015). (For interpretation of the references to colour in this figure legend, the reader is referred to the web version of this article.)

in heavy REE (HREE) with negative Eu anomalies ( $\text{Eu}/\text{Eu}^* = 0.2\text{--}0.5$ ;  $\text{Eu}^* \equiv (\text{Sm} + \text{Gd})/2$ ), although there are elevated abundances of La and Ce. Differing from this typically diagenetic orthopyroxene, the coarse-grained orthopyroxene ( $\text{En}_{71.9\text{--}72.2}\text{Fs}_{24.5\text{--}24.7}\text{Wo}_{3.2\text{--}3.6}$ ) shown in Fig. 8a has much higher REE concentrations (black patterns in Fig. 14a). The Opx-I ( $\text{En}_{54.9\text{--}59.9}\text{Fs}_{38.9\text{--}43.9}\text{Wo}_{1.2\text{--}1.4}$ ) in troilite-orthopyroxene intergrowths contains HREE concentrations comparable to those of the coarse-grained orthopyroxene shown in Fig. 8a. Different Opx-I grains in

Table 1  
Representative EPMA results (wt%) for pyroxene in NWA 7183.

	Diogenitic orthopyroxene						Troilite-opx intergrowth					Eucritic pigeonite shown in Fig. 3			
	Core			Rim			Opx-I		Opx-II						
SiO <sub>2</sub>	53.0	53.1	53.7	50.5	52.0	51.7	52.0	52.5	52.6	53.0	51.0	50.6	50.3	49.1	
TiO <sub>2</sub>	0.14	0.11	0.09	0.16	0.35	0.12	0.08	0.03	0.06	0.06	0.03	0.23	0.28	0.32	
Al <sub>2</sub> O <sub>3</sub>	1.01	1.15	0.91	1.10	0.68	0.93	0.17	0.09	0.07	0.05	0.04	1.07	0.93	0.60	
Cr <sub>2</sub> O <sub>3</sub>	0.64	0.72	0.75	0.36	0.43	0.40	0.08	0.03	0.04	0.05	0.03	0.64	0.79	0.27	
MgO	25.7	26.1	25.9	19.16	21.5	22.6	19.4	21.3	22.2	23.3	22.5	18.6	16.6	13.6	
FeO	17.4	15.8	16.2	25.9	22.2	21.3	26.4	24.7	23.8	23.0	25.5	23.9	25.7	28.7	
MnO	0.54	0.56	0.54	0.85	0.75	0.63	0.94	0.76	0.77	0.72	0.75	0.87	0.83	1.02	
CaO	1.10	1.63	1.22	1.10	1.37	1.25	0.71	0.56	0.54	0.37	0.33	3.88	4.51	4.88	
Total	99.53	99.17	99.31	99.13	99.28	98.97	99.78	99.97	99.67	100.6	100.2	99.79	99.94	98.49	
	<i>Calculated on the basis of 6 oxygen atoms</i>														
Si	1.946	1.945	1.962	1.944	1.961	1.948	1.985	1.981	1.974	1.971	1.935	1.935	1.941	1.958	
Ti	0.004	0.003	0.002	0.005	0.010	0.003	0.002	0.001	0.002	0.002	0.001	0.007	0.008	0.010	
Al	0.044	0.050	0.039	0.050	0.030	0.041	0.008	0.004	0.003	0.002	0.002	0.048	0.042	0.028	
Cr	0.019	0.021	0.022	0.011	0.013	0.012	0.002	0.001	0.001	0.001	0.001	0.019	0.024	0.008	
Mg	1.415	1.434	1.421	1.107	1.216	1.278	1.111	1.207	1.250	1.300	1.280	1.067	0.961	0.813	
Fe	0.532	0.482	0.495	0.831	0.698	0.668	0.840	0.775	0.744	0.713	0.806	0.762	0.827	0.954	
Mn	0.017	0.017	0.017	0.028	0.024	0.020	0.030	0.024	0.024	0.023	0.024	0.028	0.027	0.034	
Ca	0.043	0.064	0.048	0.045	0.055	0.050	0.029	0.023	0.022	0.015	0.013	0.159	0.187	0.208	
Sum	4.019	4.017	4.006	4.021	4.007	4.024	4.008	4.016	4.020	4.027	4.062	4.025	4.017	4.013	
Mg#	72.7	74.8	74.2	57.1	63.5	65.7	56.9	60.9	62.7	64.6	61.4	58.3	53.8	46.0	
Fe/Mn	31.8	27.8	29.6	30.0	29.2	33.1	27.7	32.0	30.5	31.5	33.5	27.1	30.5	27.7	
En	71.1	72.4	72.4	55.8	61.8	64.0	56.1	60.2	62.0	64.1	61.0	53.7	48.7	41.2	
Fs	26.7	24.4	25.2	41.9	35.4	33.5	42.4	38.6	36.9	35.2	38.4	38.3	41.9	48.3	
Wo	2.2	3.2	2.4	2.3	2.8	2.5	1.5	1.1	1.1	0.7	0.6	8.0	9.5	10.6	

Mg# = 100 \* Mg/(Mg + Fe) in mole.

En = 100 \* Mg/(Mg + Fe + Ca); Fs = 100 \* Fe/(Mg + Fe + Ca); Wo = 100 \* Ca/(Mg + Fe + Ca).

Bd: below detection limit.

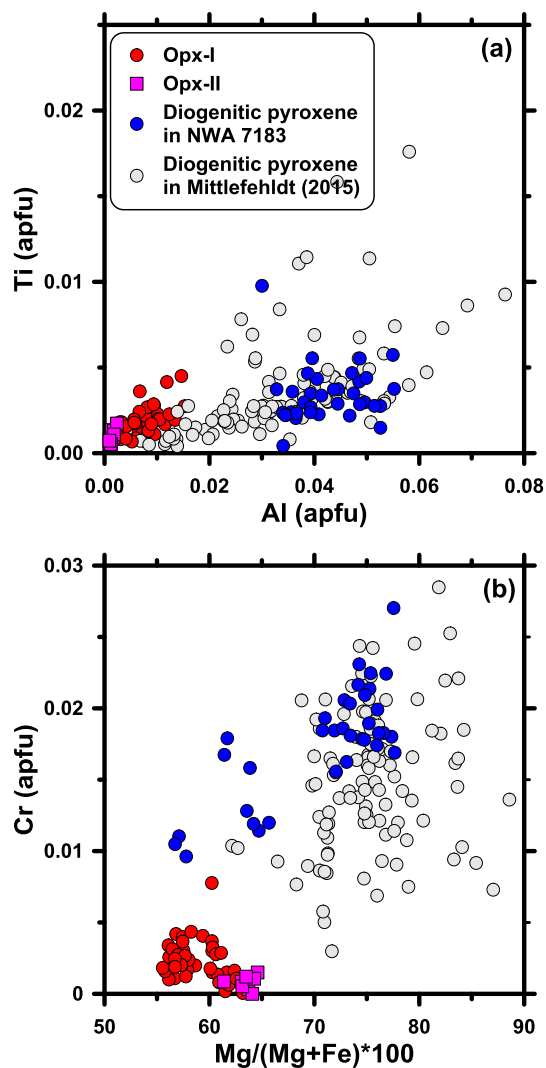


Fig. 12. Chemical compositions of minor elements (Ti, Al, and Cr) of low-Ca pyroxene in diagenetic clasts and the troilite-orthopyroxene intergrowth from NWA 7183.

the troilite-orthopyroxene intergrowths show variations in HREE by a factor of 2. However, the Opx-I shows an anomalous enrichment in light REE (LREE) and positive Eu anomalies (red patterns in Fig. 14a), which is also observed in typically diagenetic orthopyroxene with cracks and fine-grained olivine during the REE measurements in this study (not shown in this paper). This anomalous enrichment in LREE and Eu observed in Opx-I could be due to contamination during sample preparation or in the Northwest African desert and is excluded from the discussion.

Compositions of rare earth elements in a few eucritic pigeonite grains in NWA 7183 were also measured for comparison. Two pigeonite fragments, with compositions of  $\text{En}_{48.7}\text{Fs}_{41.9}\text{Wo}_{9.5}$  and  $\text{En}_{53.6}\text{Fs}_{38.4}\text{Wo}_{8.0}$ , have various REE concentrations and Eu anomalies ( $\text{Eu}/\text{Eu}^* = 0.2\text{--}0.5$ ; orange and green patterns in Fig. 14b). Although both grains are HREE-enriched, they differ greatly in LREE.

The other two data are from two pigeonite grains ( $\text{En}_{41.1\text{--}41.2}\text{Fs}_{46.3\text{--}48.3}\text{Wo}_{10.6\text{--}12.6}$ ) within a cumulate eucritic clast. They have high REE concentrations and exhibit strong negative Eu anomalies ( $\text{Eu}/\text{Eu}^* = 0.1\text{--}0.3$ ; desert blue patterns in Fig. 14b; Table 4).

### 3.4. Siderophile and chalcophile elements in troilite

Six measurements were performed on the troilite in troilite-Opx-I intergrowths. The fine-grained troilite closely associated with Opx-II was not measured, considering potential contaminations from surrounding troilite associated with Opx-I due to the hole of  $\sim 30\ \mu\text{m}$  during LA-ICP-MS measurements. Two irregular troilite grains, which are associated with Fe-Ni metal (that now has been altered to Fe-hydroxide), in a typical diagenetic lithic clast were also measured for comparison. Most of the siderophile and chalcophile elements (Os, Ir, Ru, Rh, Pd, Pt, Au, As, Te, Sb, and Bi) were not detected in either type of troilite. This result indicates that the concentrations of these elements are lower than their detection limits (2.3 ppm for Os, 0.4 ppm for Ir, 0.3 ppm for Ru, 0.06 ppm for Rh, 0.3 ppm for Pd, 0.7 ppm for Pt, 0.2 ppm for Au, 3.0 ppm for As, 5.4 ppm for Te, 0.3 ppm for Sb, and 0.1 ppm for Bi). One of the six measurements on troilite in the intergrowth shows a Se concentration below the detection limit (8.7 ppm). However, the other five measurements show Se signals slightly higher than the background. Their Se concentrations are approximately 30 to 60 ppm. The troilite grains in the typical diagenetic lithic clast contain 38–47 ppm Se.

## 4. DISCUSSION

Most of the lithic clasts and mineral fragments in NWA 7183 show petrographic textures similar to those described in howardites and brecciated diogenites (Hewins, 1981; Patzer and McSween, 2012; Eckley et al., 2016). However, some of the orthopyroxene, olivine, and chromite grains in NWA 7183 show compositional ranges different from those in typical diogenites or diagenetic clasts (Mittlefehldt, 2015). Therefore, we first discuss possible effects on the major and trace elements in these silicate and oxide minerals from terrestrial weathering and post-magmatic processes on the parent body. Then, we discuss the origin of the troilite-orthopyroxene intergrowth and its implications for the petrogenesis of diogenites.

### 4.1. Effects of terrestrial alteration on REE in low-Ca pyroxene from NWA 7183

Previous investigations demonstrated that the chemical features of meteorites from cold and hot deserts could have been altered to various degrees, although visible mineralogical evidence was not always observed (Floss and Crozaz, 1991; Barrat et al., 1999, 2015; Crozaz and Wadhwa, 2001; Crozaz et al., 2003; Hyde et al., 2014). Systematic investigations by Crozaz et al. (2003) revealed that low-Ca pyroxene and olivine are the two minerals readily affected by terrestrial weathering, with enrichment in LREE. They also noted that the LREE contamination is

Table 2

Representative EPMA results (wt%) of olivine and chromite in diagenetic clasts and the troilite-orthopyroxene intergrowth.

Olivine								Chromite				
Diagenetic clast				Tro-opx intergrowth				Diagenetic clast		Tro-opx intergrowth		
SiO <sub>2</sub>	34.7	36.5	36.4	33.1	33.7	34.5	34.3	SiO <sub>2</sub>	0.03	0.03	0.21	0.07
TiO <sub>2</sub>	bd	0.03	bd	bd	bd	bd	bd	TiO <sub>2</sub>	1.29	1.44	1.86	2.32
Al <sub>2</sub> O <sub>3</sub>	bd	bd	bd	bd	bd	0.02	bd	Al <sub>2</sub> O <sub>3</sub>	16.1	14.1	11.9	10.2
Cr <sub>2</sub> O <sub>3</sub>	0.08	0.10	0.09	bd	bd	bd	0.02	Cr <sub>2</sub> O <sub>3</sub>	48.3	49.8	49.5	52.2
MgO	25.3	35.2	34.7	17.5	18.4	24.6	25.2	MgO	1.28	1.00	1.02	1.08
FeO	38.8	27.5	26.8	48.5	46.8	40.7	40.4	FeO	32.8	32.4	34.2	33.7
MnO	0.76	0.55	0.54	1.10	1.04	0.88	0.80	MnO	0.66	0.62	0.70	0.66
CaO	bd	0.02	bd	bd	bd	bd	bd	CaO	0.16	0.16	0.07	0.17
Total	99.64	99.9	98.53	100.2	99.94	100.7	100.7	Total	100.6	99.55	99.46	100.4
<i>Calculated on the basis of 4 oxygen atoms</i>												
Si	0.987	0.977	0.986	0.990	0.998	0.981	0.975	Si	0.001	0.001	0.007	0.002
Ti	bd	0.001	bd	bd	bd	bd	bd	Ti	0.033	0.037	0.049	0.061
Al	bd	bd	bd	bd	bd	0.001	bd	Al	0.643	0.577	0.493	0.421
Cr	0.002	0.002	0.002	bd	bd	bd	0.000	Cr	1.297	1.362	1.378	1.448
Mg	1.082	1.414	1.408	0.785	0.820	1.051	1.074	Mg	0.065	0.052	0.054	0.057
Fe	0.922	0.614	0.605	1.207	1.156	0.964	0.955	Fe	0.931	0.938	1.003	0.985
Mn	0.018	0.012	0.012	0.028	0.026	0.021	0.019	Mn	0.019	0.018	0.021	0.020
Ca	bd	0.001	bd	bd	bd	bd	bd	Ca	0.006	0.006	0.002	0.006
Sum	3.011	3.021	3.013	3.010	3.000	3.018	3.023		2.995	2.991	3.007	3.000
Mg#	54.0	69.7	69.9	39.4	41.5	52.2	52.9	Mg#	6.6	5.2	5.1	5.5
Fe/Mn	50.7	49.6	49.4	43.5	44.5	45.7	49.9	Chr	64.7	67.6	70.0	72.7
Fa	54.0	69.7	69.9	39.4	41.5	52.2	52.9	Spl	32.1	28.6	25.0	21.2
								Usp	3.3	3.7	5.0	6.1

Mg# = 100 \* Mg/(Mg + Fe) in mole.

Fa = 100 \* Fe/(Mg + Fe). Chr = 100 \* Cr/(Cr + Al + 2Ti); Spl = 100 \* Al/(Cr + Al + 2Ti); Usp = 100 \* 2Ti/(Cr + Al + 2Ti).

Bd: below detection limit.

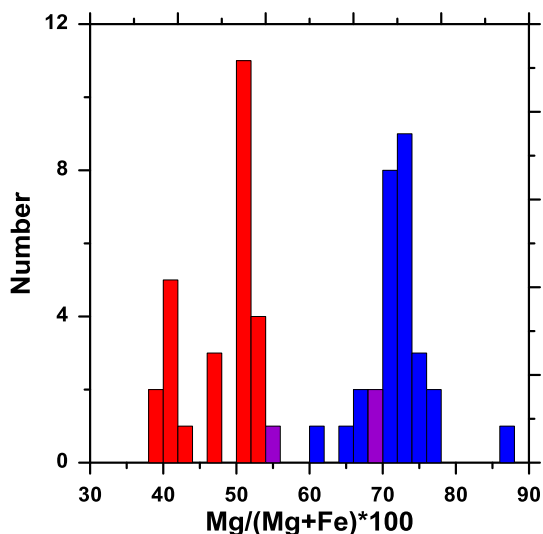


Fig. 13. Histogram of Mg/(Mg + Fe) \* 100 for olivine in NWA 7183. Red denotes olivine observed in troilite-orthopyroxene intergrowths, purple denotes diagenetic olivine in NWA 7183, and blue denotes olivine in diagenetic clasts compiled in Mittlefehldt (2015). (For interpretation of the references to colour in this figure legend, the reader is referred to the web version of this article.)

highly heterogeneous among different grains of a given mineral and even within a single grain (Croaz et al., 2003). In this study, similar LREE enrichments (particularly in La

and Ce) are also observed in some grains of the diagenetic and eucritic pyroxenes from NWA 7183 (Fig. 14). Here, we suggest that the observed enrichment of LREE in some of the low-Ca pyroxene grains in NWA 7183 could be due to terrestrial alteration in the hot Northwest Africa desert. The alteration of troilite and Fe-Ni metal grains in a few lithic clasts supports the conclusion that terrestrial alteration has affected NWA 7183. Compared with the LREE, the concentrations of HREE in pyroxenes in NWA 7183 appear to be unaffected by terrestrial alteration (Croaz et al., 2003).

#### 4.2. Post-magmatic Mg-Fe interdiffusion in the parent body

As noted above, some of the diagenetic orthopyroxene, olivine, and chromite in NWA 7183 show anomalous Fe enrichment compared with their counterparts in other HED meteorites (Mittlefehldt, 2015). First, some of the diagenetic orthopyroxene grains are Fe-enriched along the rims and fractures compared with the compositional range for diagenetic orthopyroxene compiled in Mittlefehldt (2015). The Fe enrichment along fractures excludes the possibility of magmatic zoning. Instead, it is more likely that the Fe enrichment was due to post-magmatic Mg-Fe interdiffusion. Second, chromite grains in typical diagenetic clasts in NWA 7183 are also Fe-enriched compared with those compiled in Mittlefehldt (2015). However, the chromite grains contain Ti concentrations comparable to those of typical diagenetic chromite (Mittlefehldt, 2015). Third,

Table 3  
Representative EPMA results (wt%) of troilite in troilite-orthopyroxene intergrowth in NWA 7183.

	1	3	5	6	13	15	16	17	18
S	36.7	36.2	36.7	36.6	36.4	36.0	36.3	36.6	36.5
Si	0.10	0.11	0.04	0.05	0.16	0.04	0.03	0.03	0.03
Fe	62.6	63.3	63.3	62.5	63.4	64.1	63.8	62.9	62.4
Co	0.09	0.12	0.11	0.12	0.11	0.09	0.12	0.11	0.12
Total	99.49	99.73	100.2	99.27	100.1	100.2	100.3	99.64	99.05
S/(Fe + Co)*	1.024	0.998	1.012	1.021	1.003	0.981	0.993	1.016	1.023

\* Molar ratio.

Table 4  
SIMS rare-earth element concentrations (ppm) for pyroxene in NWA 7183.

	Diogenitic orthopyroxene				Opx-I in troilite-orthopyroxene intergrowth									
	px18	1σ	px19	1σ	px08	1σ	px10	1σ	px07	1σ	px11	1σ	px12	1σ
En	73.1		73.1		59.6		59.9		56.8		54.9		57.1	
Fs	24.1		24.1		39.3		38.9		41.9		43.9		41.7	
Wo	2.8		2.8		1.2		1.2		1.4		1.2		1.2	
La	0.19	0.10	0.19	0.10	0.77	0.04	0.83	0.06	0.98	0.06	0.68	0.04	0.70	0.09
Ce	0.18	0.06	0.18	0.06	2.30	0.13	2.10	0.11	2.36	0.07	1.50	0.04	1.52	0.10
Pr	0.02	0.01	0.02	0.01	0.19	0.02	0.23	0.02	0.31	0.02	0.22	0.01	0.18	0.03
Nd	0.13	0.03	0.13	0.03	0.72	0.04	1.03	0.13	1.39	0.08	0.94	0.08	0.85	0.08
Sm	0.05	0.02	0.05	0.02	0.21	0.02	0.32	0.06	0.45	0.05	0.36	0.04	0.30	0.05
Eu	0.01	0.01	0.01	0.01	1.57	0.03	2.32	0.01	1.48	0.04	0.52	0.02	0.56	0.04
Gd	0.11	0.02	0.02	0.01	0.20	0.02	0.29	0.05	0.54	0.04	0.35	0.03	0.33	0.05
Tb	0.02	0.01	0.11	0.02	0.05	0.01	0.06	0.01	0.11	0.01	0.08	0.01	0.07	0.01
Dy	0.22	0.03	0.22	0.03	0.24	0.03	0.34	0.05	0.74	0.03	0.57	0.03	0.51	0.06
Ho	0.04	0.01	0.04	0.01	0.07	0.01	0.08	0.01	0.17	0.01	0.11	0.01	0.14	0.01
Er	0.12	0.02	0.12	0.02	0.42	0.05	0.38	0.05	0.57	0.06	0.33	0.03	0.45	0.06
Tm	0.02	0.01	0.02	0.01	0.07	0.02	0.09	0.02	0.11	0.01	0.05	0.01	0.10	0.01
Yb	0.22	0.02	0.22	0.02	0.22	0.02	0.32	0.04	0.82	0.06	0.51	0.03	0.57	0.05
Lu	0.03	0.01	0.03	0.01	0.04	0.01	0.05	0.01	0.10	0.01	0.06	0.01	0.10	0.01

	Diogenitic orthopyroxene shown in Fig. 8a with a troilite-orthopyroxene inclusion				Eucritic pigeonite grains in NWA 7183									
	px02	1σ	px11	1σ	px01	1σ	px02	1σ	px06	1σ	px09	1σ	px10	1σ
En	71.9		72.2		53.3		53.6		48.7		41.1		41.2	
Fs	24.5		24.7		38.5		38.4		41.9		46.3		48.3	
Wo	3.6		3.2		8.3		8.0		9.5		12.6		10.6	
La	0.16	0.02	0.22	0.03	0.09	0.03	0.08	0.02	0.13	0.02	0.2	0.05	0.16	0.05
Ce	0.75	0.14	1.02	0.11	0.10	0.02	0.13	0.02	0.41	0.06	0.61	0.05	0.48	0.04
Pr	0.17	0.02	0.18	0.01	0.02	0.01	0.02	0.01	0.10	0.01	0.14	0.01	0.13	0.01
Nd	0.71	0.05	0.86	0.04	0.09	0.01	0.11	0.03	0.60	0.03	0.87	0.07	0.84	0.05
Sm	0.27	0.03	0.36	0.03	0.07	0.02	0.07	0.01	0.34	0.03	0.54	0.05	0.48	0.05
Eu	0.05	0.01	0.07	0.01	0.01	0.01	0.02	0.01	0.04	0.01	0.02	0.01	0.02	0.01
Gd	0.34	0.02	0.44	0.02	0.17	0.01	0.15	0.02	0.44	0.03	0.78	0.03	0.84	0.04
Tb	0.07	0.01	0.10	0.01	0.04	0.01	0.05	0.01	0.10	0.01	0.19	0.01	0.19	0.01
Dy	0.53	0.04	0.82	0.04	0.40	0.03	0.50	0.04	0.96	0.05	1.83	0.05	1.82	0.07
Ho	0.11	0.01	0.14	0.01	0.11	0.01	0.11	0.01	0.20	0.02	0.40	0.01	0.39	0.02
Er	0.38	0.03	0.46	0.03	0.38	0.04	0.49	0.03	0.65	0.05	1.26	0.06	1.26	0.06
Tm	0.05	0.01	0.08	0.01	0.09	0.01	0.08	0.01	0.12	0.01	0.19	0.01	0.22	0.01
Yb	0.47	0.04	0.55	0.03	0.55	0.04	0.59	0.03	0.93	0.05	1.48	0.06	1.45	0.06
Lu	0.08	0.01	0.09	0.01	0.10	0.01	0.08	0.01	0.14	0.01	0.23	0.02	0.23	0.01

some of the rounded olivine grains located at the Fe-rich margins of typical diogenitic pyroxene grains in NWA 7183 are richer in Fe than those compiled in [Mittlefehldt \(2015\)](#). However, the rounded olivine grains that are included in typical diogenitic pyroxene far away (>20 μm)

from the Fe-rich margin have Mg# values comparable to those compiled in [Mittlefehldt \(2015\)](#). These observations indicate that chromite and some of the pyroxene and olivine in typical diogenitic clasts have been affected by post-magmatic Mg-Fe interdiffusion.

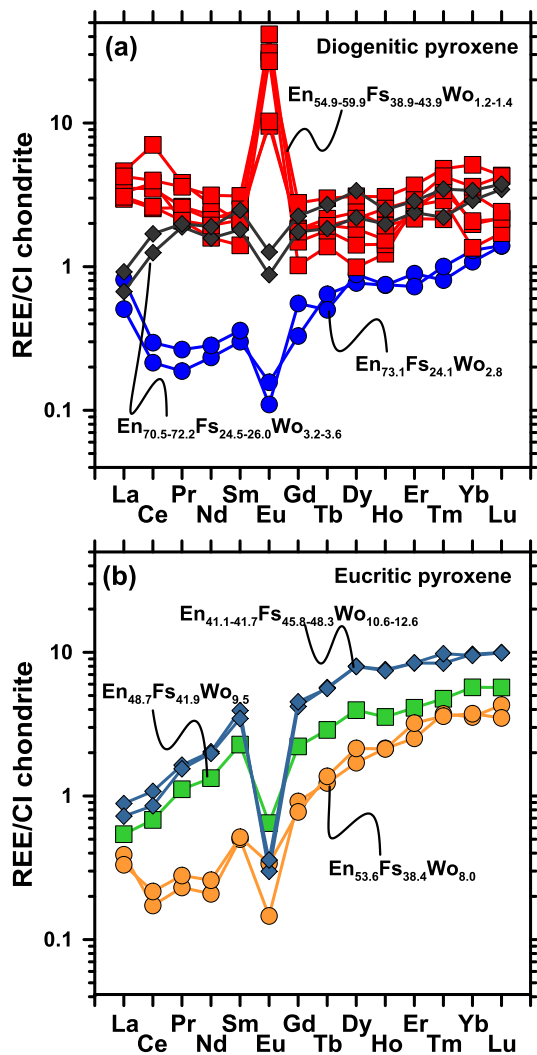


Fig. 14. REE patterns of pyroxenes in troilite-orthopyroxene intergrowth (red), diagenitic clasts (blue and pink), and eucritic clasts (orange, green, and desert blue) from Northwest Africa 7183. Reference chondrite data is from [Anders and Grevesse \(1989\)](#). (For interpretation of the references to colour in this figure legend, the reader is referred to the web version of this article.)

Troilite-orthopyroxene intergrowths have been reported in a few HED meteorites ([Hewins, 1981](#); [Patzner and McSween, 2012](#); [Eckley et al., 2016](#)). Compared with these orthopyroxene grains in the intergrowths ( $Mg\# = 64\text{--}88$ ; [Patzner and McSween, 2012](#); [Eckley et al., 2016](#)), both Opx-I and Opx-II in NWA 7183 are Fe-rich but have various  $Mg\#$  values. If these troilite-orthopyroxene intergrowths have a common source, the Fe enrichment of orthopyroxene in the intergrowths from NWA 7183 and some of those reported in [Patzner and McSween \(2012\)](#) might also have been caused by post-magmatic Mg-Fe interdiffusion. All of the olivine grains in the troilite-orthopyroxene intergrowths have  $Mg\#$  values (39–53) lower than those (66–72) reported in [Eckley et al. \(2016\)](#); meanwhile, the chromite grains in the troilite-orthopyroxene intergrowths in NWA 7183 are also more

Fe-enriched than those in typical diagenitic clasts ([Mittlefehldt, 2015](#)). Considering that the Mg-Fe interdiffusion rate in olivine and chromite is faster than that in orthopyroxene ([Dohmen et al., 2016](#)) and that the grain sizes of Opx-I and Opx-II are similar to or smaller than the width of Fe-enriched rims on typical diagenitic orthopyroxene, it is very likely that the Fe-rich features of silicate and oxide minerals in the troilite-orthopyroxene intergrowths are also due to the post-magmatic Mg-Fe interdiffusion event. Based on the compositions of Opx-I and associated olivine and chromite in a fragment of troilite-orthopyroxene intergrowth, the metamorphic temperature is  $546\text{ }^{\circ}\text{C}$  with an oxygen fugacity of  $IW+0.06$ , assuming one atmospheric pressure ([Sack and Ghiorso, 1989, 1991a, 1991b, 1994a, 1994b, 1994c](#)).

Differing from major elements Mg and Fe in the Fe-enriched orthopyroxene in NWA 7183, the concentrations of minor elements Cr, Ti, and Al appear unaffected by the post-magmatic process. On one hand, the chemical ranges of Cr, Ti, and Al in diagenitic orthopyroxene from NWA 7183 are most consistent with those reported in the literature ([Mittlefehldt, 2015](#)). On the other hand, although Opx-I and Opx-II have  $Mg\#$  values comparable to those of Fe-enriched rims of diagenitic orthopyroxene, they have Cr, Ti, and Al concentrations differing from those in the Fe-enriched diagenitic orthopyroxene. Therefore, the low concentrations of Cr, Ti, and Al in Opx-I and Opx-II should be primitive features, rather than due to post-magmatic processes, or at least not due to the same process that resulted in Fe-Mg interdiffusion in orthopyroxene, olivine, and chromite.

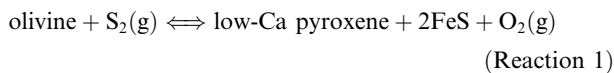
#### 4.3. Metasomatic origin of the troilite-orthopyroxene intergrowth

Only the origin of the intergrowth that is similar to the troilite-Opx-I intergrowth in this study has been discussed. In this study, we observe two types of troilite-orthopyroxene intergrowths (troilite-Opx-I and troilite-Opx-II). They share some similarities in texture and mineral assemblage, but two features distinguish Opx-II from Opx-I. First, Opx-II and associated troilite are smaller in grain size than Opx-I and its associated troilite ([Figs. 4f and 8b and c](#)). Second, Opx-II has  $Mg\#$  values slightly higher than Opx-I, while the Wo components in Opx-I are slightly higher than those in Opx-II ([Table 1 and Fig. 12](#)). These two differences indicate that Opx-II and Opx-I formed at two different stages; otherwise, they would have identical compositions, including  $Mg\#$  values and Cr, Al, and Ca concentrations. The different  $Mg\#$  values of Opx-I and Opx-II also argue against the possibility that both Opx-I and Opx-II formed prior to the post-magmatic Mg-Fe interdiffusion event. Therefore, given that some of the Opx-I are Fe-enriched to an extent similar to that of the Fe-rich rim of typical diagenitic orthopyroxene in NWA 7183 ([Fig. 11](#)), we suggest that the formations of Opx-I and Opx-II might predate and postdate the post-magmatic Mg-Fe interdiffusion event, respectively, and we discuss their origins separately.

#### 4.3.1. The troilite-Opx-II intergrowth

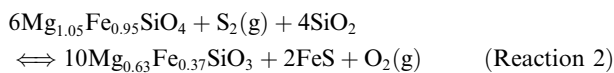
The troilite-Opx-II intergrowth is observed in only two lithic clasts in NWA 7183, and its constituent minerals are very fine-grained. Therefore, we discuss its origin based on the texture and chemical compositions of major and minor elements.

The Opx-II and related finer-grained troilite, exhibiting an intimate intergrowth texture, are closely associated with relatively large, irregular olivine grains (Eckley et al., 2016; Figs. 4f and 8b and c in this study). Such texture is similar to the sulfide replacement textures in Apollo samples 67016 and 67915 (Roedder and Weiblen, 1974; Norman, 1981; Norman et al., 1995; Shearer et al., 2012) and in the ungrouped achondrite Divnoe (Petaev et al., 1994). In the literature (Norman, 1981; Petaev et al., 1994; Norman et al., 1995; Shearer et al., 2012), this replacement texture has been interpreted by the general reaction:

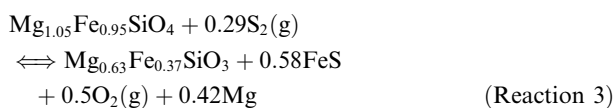


In this study, reaction (1) can also account for the observed texture for Opx-II and fine-grained troilite in NWA 7183. Meanwhile, such an explanation based on the petrographic texture is supported chemically by the low concentrations of Cr, Al, Ti, and Ca in Opx-II. Since olivine is depleted in Cr, Al, Ti, and Ca, the reaction product low-Ca pyroxene would be depleted in these elements, compared with those crystallized from normal mafic or ultramafic magmas (Petaev et al., 1994). This inference is very consistent with the observation in this study that Opx-II has lower concentrations of Cr, Al, Ti, and Ca than typical diagenitic orthopyroxene (Figs. 11 and 12).

In reaction (1), the formation of troilite extracts Fe from olivine and results in the increase of the Mg# value in the reaction product low-Ca pyroxene. This effect is qualitatively consistent with observations in NWA 7183 (e.g., mean Mg# value 0.53 in olivine, mean Mg# value 0.63 in Opx-II). However, to quantitatively explain the chemical compositions of Opx-II and its related olivine, the addition of SiO<sub>2</sub> to the reactant or the loss of Mg from the system would be required to balance the equation, based on the following two reactions:



and



Similar reactions have been proposed to interpret the compositions of minerals in the replacement texture of olivine by orthopyroxene and troilite in Apollo samples (Shearer et al., 2012). Each reaction indicates that the sulfidation of olivine is not open only to S and that other elements (e.g., Mg and Fe) should also be involved (Shearer et al., 2012). For example, Shearer et al. (2012) revealed that Se, Cu, Zn, and Sb have also been transported into the replacement texture of olivine by troilite and orthopy-

roxene, although the reactions were not controlled by the behaviors of these trace elements in the reactions. For the sulfidation of Fe-rich pigeonite in the brecciated eucrite NWA 2339, Zhang et al. (2013) revealed that Mn in the system was partially lost during sulfidation based on X-ray mapping of Mn. For simplicity, we suggest that during the formation of Opx-II, some Mg might have been lost from the system (c.f., Shearer et al., 2012), although no Mg-rich phase associated with the intergrowths is observed in this study.

#### 4.3.2. The troilite-Opx-I intergrowth

A few fragments of troilite-orthopyroxene intergrowth have been reported from howardite and brecciated diogenites in previous studies (Hewins, 1981; Patzer and McSween, 2012; Eckley et al., 2016). Their textures and mineral assemblages are similar to the troilite-Opx-I intergrowth in this study, indicating that they might have a common origin.

Patzer and McSween (2012) stated that the troilite-orthopyroxene intergrowth should be restricted to harzburgitic lithologies, based on the petrographic texture and Mg-rich nature of orthopyroxene. In this study, we observe that olivine is commonly included in Opx-I. This result implies that the troilite-orthopyroxene intergrowth could be related in origin to an olivine-bearing or olivine-rich lithology. In addition, the fine-grained chromite that is included in Opx-I contains very low ulvöspinel contents, similar to those of diagenitic chromite and largely different from those of eucritic chromite (Fig. 7 in Mittlefehldt, 2015). This relationship implies that the origin of troilite-orthopyroxene intergrowths should be closely associated with diogenite rather than eucrite. However, Opx-I in the troilite-orthopyroxene intergrowths is depleted in Cr, Al, and Ti, distinct from typical diagenitic orthopyroxene (Fig. 12). This chemical feature argues against a simple diagenitic origin for the troilite-orthopyroxene intergrowths in HED meteorites.

Two scenarios have been proposed to interpret the origin of troilite-orthopyroxene intergrowths in howardites and brecciated diogenites (Hewins, 1981; Patzer and McSween, 2012; Eckley et al., 2016). Patzer and McSween (2012) and Eckley et al. (2016) proposed that the troilite-orthopyroxene intergrowths could have formed via impact-induced melting and rapid crystallization of diagenitic orthopyroxene in the presence of troilite. Patzer and McSween (2012) drew this conclusion based on comparison of the petrographic texture of the troilite-orthopyroxene in diogenite LEW 88679 and in the Aca-pulco meteorite (El Goresy et al., 2005). If this were the case, because Cr, Al, Ti, and Ca are lithophile elements that are usually incompatible in troilite, the presence of troilite would not affect the concentrations of Cr, Al, Ti, and Ca in orthopyroxene before and after shock-induced localized melting. Unfortunately, no details about the Cr, Al, and Ti concentrations have been reported for the orthopyroxene in the intergrowths (Patzer and McSween, 2012). In our study, the Cr, Al, and Ti concentrations in Opx-I are distinctly lower than those in the typical diagenitic orthopyroxene in NWA 7183 and in the literature (Mittlefehldt,

2015). The Wo contents are also lower than those in the typical diagenetic orthopyroxene in NWA 7183 and in the literature (Mittlefehldt, 2015). This chemical difference argues against the possibility that the troilite-orthopyroxene intergrowths in NWA 7183 have formed via impact-induced localized melting and rapid crystallization of diagenetic orthopyroxene in the presence of troilite. Therefore, Opx-I is not a product of shock-induced localized melting and recrystallization of diagenetic orthopyroxene in the presence of troilite.

Hewins (1981), in his conference abstract, proposed that the troilite-orthopyroxene intergrowths could have formed via reactions between primary olivine and S-rich fluid based on their petrographic observations. This model is supported by the mineral assemblage and texture of the troilite-orthopyroxene intergrowths in this study. First, olivine usually occurs as small and irregular inclusions in Opx-I. Our observations reveal that the small olivine grains have compositions identical to those of relatively coarse-grained olivine grains within same lithic clasts. The small irregular olivine grains could be of relict origin during the reaction. The relatively coarse irregular olivine grains shown in Figs. 5e and 8a probably have a similar origin. Second, Opx-I in the intergrowths also contains lower concentrations of Cr, Al, Ti, and Ca than typical diagenetic orthopyroxene, supporting a reaction between olivine and S-rich fluid (Hewins, 1981), which is similar to the reaction interpreting the origin of troilite-Opx-II intergrowth discussed above. Thus, we suggest that troilite-Opx-I intergrowths are also products of olivine metasomatism by S-rich fluid, based on the unique compositional features (Cr, Al, Ti, and Ca) of Opx-I and the fact that relict diagenetic olivine and chromite are included in or enclosed by Opx-I.

Although we propose that both Opx-I and Opx-II are products of a reaction between olivine and S-rich fluid/vapor, the subtle differences in Cr, Al, and Ca concentrations between Opx-I and Opx-II imply certain differences for their formation conditions. To interpret such subtle differences between Opx-I and Opx-II, we suggest that Opx-I might also have formed via a peritectic reaction between olivine and S-rich vapor but at higher temperatures than those for the formation of Opx-II (c.f., Petaev et al., 1994). Petaev et al. (1994) suggested that reaction between S and olivine would result in an assemblage of molten troilite and pyroxene-rich silicate melt with as-yet-unreacted olivine if the temperature were higher than its peritectic temperature. With high temperatures, some diagenetic orthopyroxene and/or chromite might have been melted, resulting in the slightly elevated concentrations of Al, Cr, Ti, and Ca in Opx-I. In contrast, probably no diagenetic orthopyroxene and/or chromite were melted during the formation of the troilite-Opx-II intergrowths. We suggest that the reaction for the formation of troilite-Opx-I intergrowth, similar to the formation of troilite-Opx-II intergrowth, could also be open to S, Mg, and probably other elements (e.g., Se). However, it is difficult to quantitatively constrain the reaction conditions since the major element compositions of the silicate and oxide minerals have been modified in the post-magmatic Mg-Fe interdiffusion event.

The texture of the troilite-Opx-I intergrowths is similar to that of magmatic sulfide-silicate intergrowths in magmatic sulfide ore deposits (Barnes et al., 2017), supporting the idea that the troilite-Opx-I intergrowth probably crystallized from a high-temperature melt. The simultaneous crystallization of Opx-I and associated troilite is also supported by the continuity of crystallographic orientations of Opx-I and troilite grains within single lithic clasts or certain regions (Figs. 5 and 6). In addition, the crystallization model for Opx-I and its associated troilite from high-temperature melt can also explain the texture where the intergrowth partly encloses a grain of diagenetic orthopyroxene with a smooth boundary (Fig. 9).

Some of the troilite grains in intergrowths from NWA 7183 have an interconnecting texture (Fig. 4a), imposing a possibility that the igneous texture of troilite-Opx-I intergrowths might have formed through the infiltration of troilite into preexisting orthopyroxene. However, two aspects of consideration argue against this possibility in NWA 7183. First and most importantly, the infiltration model itself cannot account for the depletion of Cr, Al, Ti, and Ca in Opx-I, compared with typical diagenetic orthopyroxene (Mittlefehldt, 2015; this study). Second, synthetic experiments have revealed that the segregation velocity of Fe-S melt in unmolten peridotite is very low due to the high surface tension of sulfide (Bagdassarov et al., 2009). This result indicates that infiltration of troilite into preexisting orthopyroxene is not an efficient process to form the observed texture.

Chalcophile and siderophile elements in sulfide have been measured to distinguish S-rich vapor from S-rich melt during mantle metasomatism of the Earth (Lorand et al., 2004; Delpech et al., 2012). The principle is that mantle metasomatism by S-rich vapors would fractionate chalcophile and siderophile elements (Delpech et al., 2012) proportional to their volatility order ( $S > Se > Te > As$ ,  $Au > Pd > Ir > Os$ ; Lodders, 2003). However, mantle metasomatism by S-rich melt would not cause any fractionation among the chalcophile and siderophile elements (e.g., Lorand et al., 2004; Delpech et al., 2012). In this study, a few chalcophile and siderophile elements have been measured in the troilite in the intergrowths. However, most of the chalcophile and siderophile elements have concentrations below detection limits, except for Se. Considering that Se in sulfide from terrestrial rocks is sensitive to weathering (Lorand and Luguet, 2016), the measured Se concentrations in troilite of this study may not reflect the original concentrations. Two observations support this inference. First, some Fe-Ni metal and sulfide grains in NWA 7183 have been partly altered. Second, troilites with different origins in this study have comparable Se concentrations. To be conservative, the measured concentrations of the chalcophile and siderophile elements in troilite neither support nor preclude the sulfidation model involving S-rich vapor.

#### 4.4. Conditions for the sulfidation reaction of olivine

The reaction between olivine and sulfur has been studied experimentally and theoretically (Kullerud and Yoder,

1963, 1964; Colson, 1992; Bataleva et al., 2016). Among them, Kullerud and Yoder (1963, 1964) and Bataleva et al. (2016) studied the reaction under high pressures and high temperatures (2000 bars and 650–800 °C and 6.3 GPa and 1050–1550 °C, respectively). Colson (1992) mainly considered the effects of temperatures and the fugacity of S<sub>2</sub> and O<sub>2</sub>. Since the resultant texture in Bataleva et al. (2016) is significantly different from the texture of troilite-orthopyroxene intergrowths in this study and that in Shearer et al. (2012), we suggest that temperature and fugacity of S<sub>2</sub> and O<sub>2</sub> rather than pressure might be the key factors controlling the formation of orthopyroxene through replacing olivine.

If the sulfur fugacity  $f_{S_2}$  in the system is large enough, pyrite or pyrrhotite would be the stable sulfide phase (Toulmin and Barton, 1964) rather than troilite. Troilite is stable only at low  $f_{S_2}$  in equilibrium with native iron (Toulmin and Barton, 1964). In this study, a few fine-grained Fe-Ni metal grains are observed in some fragments of the troilite-orthopyroxene intergrowth (Figs. 4c, e, and 8b), supporting the relatively low sulfur fugacity during the reaction. However, the Fe-Ni metal grains are rare in the studied troilite-orthopyroxene intergrowths and have a chemical composition (i.e., ~1.7 wt% Ni) identical to those grains that are not associated with the troilite-orthopyroxene intergrowths, indicating that the Fe-Ni metal grains are not a byproduct during the sulfidation of olivine. Therefore, the Fe-Ni metal might not be the predominant phase for balancing the sulfur and oxygen fugacities. We suspect that the sulfur and oxygen fugacities during the sulfidation reaction of olivine might have also been controlled by the compositions of orthopyroxene in the intergrowth. However, unfortunately, the troilite-Opx-I intergrowths have been affected by the post-magmatic Mg-Fe interdiffusion event, as discussed above. The oxygen fugacity during the post-magmatic Mg-Fe interdiffusion might not have been identical to that during the sulfidation reaction of olivine to orthopyroxene. If we take the oxygen fugacity (IW–2.5) at 2000 bars and 1000 °C of NWA 5480 (Peslier et al., 2015), which is an olivine-rich diogenite, and assume that the Fa content of olivine is 0.3, the sulfur fugacity  $\log f_{S_2}$  during sulfidation of olivine is approximately –7.9 based on the calibration reaction in Egglar and Lorand (1993).

#### 4.5. Potential source of S-rich vapors

Troilite is a common accessory mineral in HED meteorites (McSween et al., 2011; Mittlefehldt, 2015). Its abundance in diogenite meteorites is usually less than 3 vol%. This is consistent with the model that metal-sulfide segregated from the silicate melt and formed the core of Vesta during the earliest stage of Vesta's evolution (McSween et al., 2011). The low abundance of troilite in diogenite meteorites makes the source of sulfur for the reaction a mystery. It might have an exotic source (e.g., chondrite) or a hidden source in the interior of Vesta. In this study, troilite associated with Opx-I and that in typical diogenitic clasts have identically low concentrations of siderophile and chalcophile elements (below detection limits), similar to

those measured in Day et al. (2012). This similarity implies that the sulfur for the metasomatic reaction of olivine might have been derived from a source from the interior of Vesta. If this is the case, the formation of S-rich vapor could be due to igneous degassing on Vesta or impact-induced vaporization of S-rich material from Vesta's interior.

Although no data of siderophile and chalcophile elements in troilite from chondrites have been reported to date using LA-ICP-MS, their concentrations in troilite could also be below the detection limits by LA-ICP-MS since Fe-Ni metal usually occurs as the predominant carrier of highly siderophile elements in chondrites. This increases the complexity for understanding the potential source of sulfur. If the S-rich vapor has an exotic origin (e.g., chondrite), it is very likely that S-rich vapor was shock-induced. In this study, the current data cannot distinguish the two potential sources of sulfur. Thus, open questions remain as to where the S sources were and how the S-rich vapors formed on Vesta. Answering these questions requires future development of analyses with lower detection limits for chalcophile and siderophile elements.

#### 4.6. Implication for diverse petrogenesis of diogenite

As discussed above, the presence of relict olivine and chromite indicates that the formation of the troilite-orthopyroxene intergrowth should be later than that of olivine-bearing/-rich diogenite. However, one lithic clast in this study shows that the troilite-orthopyroxene intergrowth is entirely enclosed by diogenitic orthopyroxene grains (Fig. 8a). There are two possibilities for interpreting this texture. One possibility is that the troilite-orthopyroxene intergrowth was trapped as a melt by growing diogenitic orthopyroxene. In this case, the enclosed melt that corresponds to the troilite-orthopyroxene intergrowth would equilibrate in Cr, Al, Ti, and Ca with the melt from which diogenitic orthopyroxene crystallized, due to fast diffusion rates in high-temperature melts (Zhang, 2010). As a consequence, Opx-I should have Cr, Al, Ti, and Ca concentrations similar to those in diogenitic orthopyroxene. However, this interpretation is contrary to the observations in this study. Therefore, it is unlikely that the troilite-orthopyroxene intergrowth shown in Fig. 8a was trapped as a melt by diogenitic orthopyroxene. Instead, it is more likely that the troilite-orthopyroxene intergrowth was captured as a solid xenolith during the crystallization of diogenitic orthopyroxene. The initial sizes of the xenoliths could be larger than those observed in this study. However, the outer parts of the original xenoliths could have been melted by surrounding diogenitic melts, resulting in the curved shape of the relict troilite-orthopyroxene intergrowth. This process might be similar to that for the formation of rounded olivine included in orthopyroxene. The comparable HREE concentrations of the orthopyroxene between the troilite-orthopyroxene intergrowth and surrounding diogenitic orthopyroxene support such an interpretation, although it is not definitive. If this is the case, this texture shown in Fig. 8a suggests that the diogenitic orthopyroxene grains should have formed after the formation of the troilite-orthopyroxene intergrowth. As a

consequence, the orthopyroxenitic diogenites, represented by the orthopyroxene grains shown in Fig. 8a, are not the cumulate rocks directly crystallized from the Vestan magma ocean as previously thought.

There are abundant investigations into the petrogenesis of diogenites in the literature, including observations on natural samples, laboratory experiments, and computational modeling (e.g., Stolper, 1977; Mittlefehldt, 1994, 2015; Righter and Drake, 1997; Ruzicka et al., 1997; Barrat et al., 2008, 2010; Yamaguchi et al., 2011; Mittlefehldt et al., 2012; Mandler and Elkins-Tanton, 2013; and references therein). It is widely accepted that diogenites are cumulate rocks directly crystallized from a magma ocean. Recently, however, Barrat et al. (2008, 2010) suggested that the parent melts of diogenites could have formed from the melting of the magma ocean cumulates and that some of them might have been contaminated by partial melting of the eucritic crust, based on REE geochemistry of diogenitic orthopyroxene. Yamaguchi et al. (2011) reported chemically zoned orthopyroxene in unequilibrium diogenites. They concluded that diogenites are not the products of the crystallization of the Vestan magma ocean. Instead, the diogenites could be associated with a later stage of magmatism (Yamaguchi et al., 2011). In the current study, the presence of the troilite-orthopyroxene intergrowth as an inclusion in diogenitic orthopyroxene provides important petrographic evidence for complex petrogenesis of diogenites. At least some of the diogenites, if not all, are not the cumulate rocks directly crystallized from the Vestan magma ocean as previously thought. They probably originated from melting of the magma-ocean cumulates as suggested by Barrat et al. (2008, 2010) and Yamaguchi et al. (2011).

#### 4.7. Implication for the absence of olivine at Vestan south pole basins

The magma-ocean models predict that some olivine-rich rocks are located in the deep interior of the parent body of HED meteorites (Righter and Drake, 1997; Ruzicka et al., 1997; Mandler and Elkins-Tanton, 2013). Olivine-bearing and olivine-rich diogenites have been observed in the meteorite collections, supporting the magma-ocean models (Sack et al., 1991; Beck and McSween, 2010; Beck et al., 2011). Given that asteroid 4-Vesta is the parent body of HED meteorites (Russell et al., 2012), searching olivine-rich rocks on the surface of Vesta has been started with the Visible and Infrared (VIR) Mapping Spectrometer on board the NASA's Dawn spacecraft. Such olivine-rich lithologies from the Vestan mantle were expected to be detected at the large south pole impact basins due to their great depths of ~30–50 km (Beck et al., 2013). However, no olivine-rich lithologies were detected at the two south pole basins on Vesta. Instead, some olivine-rich materials have been detected in regions that are far from the south pole basins (Ammannito et al., 2013b; Palomba et al., 2015; Le Corre et al., 2015; Nathues et al., 2015; Turrini et al., 2016). These olivine-rich materials are usually considered as having an exogenic source (Palomba et al., 2015; Le Corre et al., 2015; Nathues et al., 2015; Turrini et al., 2016).

Beck et al. (2013) simulated the detection limit of olivine with a VIR spectrometer. They found that harzburgitic diogenites with 11 and 27% olivine have spectroscopic features nearly identical to those of an orthopyroxenitic diogenite with approximately 100% orthopyroxene, indicating that a rock with an abundance of olivine <30% would be identified with difficulty. As for the non-detection of olivine at the south pole basins on Vesta, the following two main scenarios have been considered. (1) One scenario is that the primary rocks at the two basins have initial abundances of olivine lower than the lower detection limit for olivine with the VIR spectrometer. This could be because the fractional evolution of Vesta is more complex than previously thought in theoretical models (Ammannito et al., 2013b; Palomba et al., 2015). For example, the Vestan crust could be thicker than the excavation depths at the two south pole basins (Nathues et al., 2015; Turrini et al., 2016). (2) The other possibility is that original olivine-rich lithologies have been modified by later impact gardening (Beck et al., 2013). For example, olivine-rich lithologies might have physically mixed with olivine-poor lithologies during the long-term (1–2 Gyr) exposure history of south pole basins. In this study, our observations reveal that the olivine grains in diogenites could have been altered to orthopyroxene through reactions with S-rich vapors, although the exact formation mechanism of S-rich vapors remains an open question. If the sulfidation process occurred at the south pole impact basins of Vesta, some of the olivine grains might have been altered to orthopyroxene, resulting in the abundance of olivine being lower than the detection limit of the Dawn VIR spectrometer.

Although the troilite-orthopyroxene intergrowths are commonly observed in NWA 7183, the sulfidation might not be a large-scale process on Vesta. Instead, it could be a small but widespread process (Hewins, 1981; Patzer and McSween, 2012; Zhang et al., 2013; this study). It is one of the potentially efficient processes that could have decreased the abundance of olivine at the south pole basins of Vesta.

## 5. SUMMARY

- Two groups of troilite-orthopyroxene intergrowths have been observed in the brecciated diogenite NWA 7183. The majority of the troilite-orthopyroxene intergrowths are composed of troilite and orthopyroxene (Opx-I) and contain very fine-grained olivine and chromite as inclusions within orthopyroxene. The other group of intergrowths is observed in only a few fragments with a high abundance of olivine. The orthopyroxene (Opx-II) and associated troilite appear replacing olivine in texture and are finer-grained than Opx-I and associated troilite.
- Both Opx-I and Opx-II are depleted in Cr, Al, Ti, and Ca compared with diogenitic orthopyroxene. Combining this observation with the petrographic textures, we suggest that metasomatic reactions of olivine-bearing/-rich rocks with S-rich vapors could have resulted in the formation of the troilite-Opx-I intergrowths at

temperatures higher than the peritectic temperature from olivine to orthopyroxene. After that, post-magmatic Mg-Fe interdiffusion occurred in the troilite-orthopyroxene intergrowth and associated diogenitic orthopyroxene. The Mg-Fe interdiffusion event may have proceeded at a temperature of 546 °C and an oxygen fugacity of IW+0.06. Subsequent to the Mg-Fe interdiffusion event, some relict olivine grains were further altered to Opx-II by later S-rich vapors.

- The inclusion of the troilite-orthopyroxene intergrowth in diogenitic orthopyroxene indicates that the host orthopyroxenitic diogenite should have crystallized after the troilite-orthopyroxene intergrowth, arguing against an origin as cumulates directly crystallized from the magma ocean of Vesta. Instead, they could have originated from partial melting and recrystallization of the magma-ocean cumulates.
- Based on the current observations, olivine in diogenitic meteorites could have been altered into orthopyroxene. This metasomatic process can partly explain why the expected olivine-rich diogenitic rocks at the south pole basins of Vesta were not detected by the Dawn VIR imaging spectrometer.

#### ACKNOWLEDGEMENTS

The first author thanks Dr. Juan Li at Nanjing University for technical assistance during EBSD mapping and Dr. Zhihui Dai at the Institute of Geochemistry, Chinese Academy of Sciences, for technical assistance during the LA-ICP-MS measurements in this study. This work was funded by grants from Natural Science Foundation of China (41373065, 41673068), Natural Science Foundation of Jiangsu Province of China (BK20170017), and the Fundamental Research Funds for the Central Universities. Reviews by three anonymous reviewers as well as editorial comments by Associate Editor J.M.D. Day, greatly improved the manuscript.

#### REFERENCES

- Ammannito E., De Sanctis M. C., Capaccioni F., Capria M. T., Carraro F., Combe J. P., Fonte S., Frigeri A., Joy S. P., Longobardo A., Magni G., Marchi S., McCord T. B., McFadden L. A., McSween H. Y., Palomba E., Pieters C. M., Polansky C. A., Raymond C. A., Sunshine J. M., Tosi F., Zambon F. and Russell C. T. (2013a) Vestan lithologies mapped by the visual and infrared spectrometer on Dawn. *Meteorit. Planet. Sci.* **48**, 2185–2198.
- Ammannito E., De Sanctis M., Palomba E., Longobardo A., Mittlefehldt D., McSween H., Marchi S., Capria M., Capaccioni F., Frigeri A., Pieters C., Ruesch O., Tosi F., Zambon F., Carraro F., Fonte S., Giesinger H., Magni G., McFadden L., Raymond C., Russell C. and Sunshine J. (2013b) Olivine in an unexpected location on Vesta's surface. *Nature* **504**, 122–125.
- Anders E. and Grevesse N. (1989) Abundances of the elements—Meteoritics and solar. *Geochim. Cosmochim. Acta* **53**, 197–214.
- Bagdassarov N., Solferino G., Golabek G. J. and Schmidt M. W. (2009) Centrifuge assisted percolation of Fe-S melts in partially molten peridotite: time constraints for planetary core formation. *Earth Planet. Sci. Lett.* **288**, 84–95.
- Barnes S. J., Mungall J. E., Le Vaillant M., Godel B., Leshner C. M., Holwell D. A., Lightfoot P. C., Krivolutskaia N. and Wei B. (2017) Sulfide-silicate textures in magmatic Ni-Cu-PGE sulfide ore deposits: disseminated and net-textured ores. *Am. Miner.* **102**, 473–506.
- Barrat J. A. and Yamaguchi A. (2014) Comment on “The origin of eucrites, diogenites, and olivine diogenites: magma ocean crystallization and shallow magma processes on Vesta” by B. E. Mandler and L. T. Elkins-Tanton. *Meteorit. Planet. Sci.* **49**, 468–472.
- Barrat J. A., Gillet P., Lesourd M., Blichert-Toft J. and Poupeau G. R. (1999) The Tatahouine diogenite: mineralogical and chemical effects of sixty-three years of terrestrial residence. *Meteorit. Planet. Sci.* **34**, 91–97.
- Barrat J. A., Yamaguchi A., Greenwood R. C., Benoit M., Cotten J., Bohn M. and Franchi I. A. (2008) Geochemistry of diogenites: still more diversity in their parental melts. *Meteorit. Planet. Sci.* **43**, 1759–1775.
- Barrat J. A., Yamaguchi A., Zanda B., Bollinger C. and Bohn M. (2010) Relative chronology of crust formation on asteroid Vesta: insight from the geochemistry of diogenites. *Geochim. Cosmochim. Acta* **74**, 6218–6231.
- Barrat J. A., Yamaguchi A., Bunch T. E., Bohn M., Bollinger C. and Ceuleneer G. (2011) Possible fluid-rock interaction on differentiated asteroids recorded in eucritic meteorites. *Geochim. Cosmochim. Acta* **75**, 3839–3852.
- Barrat J. A., Greenwood R. C., Verchovsky A. B., Gillet Ph., Bollinger C., Langlade J. A., Liorzou C. and Franchi I. A. (2015) Crustal differentiation in the early solar system: clues from the unique achondrite Northwest Africa 7325 (NWA 7325). *Geochim. Cosmochim. Acta* **168**, 280–292.
- Bataleva Y. V., Palyanov Y. N., Borzdov Y. M. and Sobolev N. V. (2016) Sulfidation of silicate mantle by reduced S-bearing metasomatic fluids and melts. *Geology* **44**, 271–274.
- Beck A. W. and McSween H. Y. (2010) Diogenites as polymict breccias composed of orthopyroxenite and harzburgite. *Meteorit. Planet. Sci.* **47**, 850–872.
- Beck A. W., Mittlefehldt D. W., McSween H. Y., Rumble D., Lee C.-T. A. and Bodnar R. J. (2011) MIL 03443, a dunite from Asteroid 4 Vesta: evidence for its classification and cumulate origin. *Meteorit. Planet. Sci.* **48**, 1133–1151.
- Beck A. W., McCoy T. J., Sunshine J. M., Viviano C. E., Corrigan C. M., Hiroi T. and Mayne R. G. (2013) Challenges in detecting olivine on the surface of 4 Vesta. *Meteorit. Planet. Sci.* **48**, 2155–2165.
- Colson R. O. (1992) Mineralization on the Moon?: theoretical considerations of Apollo 16 “rusty rocks”, replacement in 67016, and surface-correlated volatiles on lunar volcanic glass. In *Proceedings 22nd Lunar and Planetary Science Conference*, pp. 427–436.
- Crozaz G. and Wadhwa M. (2001) The terrestrial alteration of Saharan Shergottites Dar al Gani 476 and 489: a case study of weathering in a hot desert environment. *Geochim. Cosmochim. Acta* **65**, 971–978.
- Crozaz G., Floss C. and Wadhwa M. (2003) Chemical alteration and REE mobilization in meteorites from hot and cold deserts. *Geochim. Cosmochim. Acta* **67**, 4727–4741.
- Day J. M. D., Walker R. J., Qin L. P. and Rumble, III, D. (2012) Late accretion as a natural consequence of planetary growth. *Nat. Geosci.* **5**, 614–617.
- Day J. M. D., Brandon A. D. and Walker R. J. (2016) Highly siderophile elements in Earth, Mars, the Moon, and asteroids. *Rev. Mineral. Geochem.* **81**, 161–238.
- De Sanctis M. C., Ammannito E., Capria M. T., Tosi F., Capaccioni F., Zambon F., Carraro F., Fonte S., Frigeri A., Jaumann R., Magni G., Marchi S., McCord T. B., McFadden L. A., McSween H. Y., Mittlefehldt D. W., Nathues A., Palomba E., Pieters C. M., Raymond C. A., Russell C. T.,

- Toplis and Turrini D. (2012) Spectroscopic characterization of mineralogy and its diversity across Vesta. *Science* **336**, 697–700.
- Delpech G., Lorand J.-P., Grégoire M., Cottin J.-Y. and O'Reilly S. Y. (2012) In-situ geochemistry of sulfides in highly metasomatized mantle xenoliths from Kerguelen, southern Indian Ocean. *Lithos* **154**, 296–314.
- Dohmen R., Ter Heege J. H., Becker H. W. and Chakraborty S. (2016) Fe-Mg interdiffusion in orthopyroxene. *Am. Miner.* **101**, 2210–2221.
- Eckley S. A., McSween H. Y. and Taylor L. A. (2016) Uncommon diogenitic troilite-orthopyroxene melt texture: 2-phase symplectite found in diogenite NWA 10451. In *47th Lunar and Planetary Science Conference, Abstract #2030*.
- Egglar D. H. and Lorand J. P. (1993) Mantle sulfide geobarometry. *Geochim. Cosmochim. Acta* **57**, 2213–2222.
- El Goresy A., Zinner E., Pellas P. and Caillet C. (2005) A menagerie of graphite morphologies in the Acapulco meteorite with diverse carbon and nitrogen isotopic signatures: implications for the evolution history of acapulcoite meteorites. *Geochim. Cosmochim. Acta* **69**, 4535–4556.
- Floss C. and Crozaz G. (1991) Ce anomalies in the LEW85300 eucrite: evidence for REE mobilization during Antarctic weathering. *Earth Planet. Sci. Lett.* **107**, 13–24.
- Hewins R. H. (1981) Fractionation and equilibration in diogenites. *Lunar Planet. Sci. XII*, 445–447.
- Hyde B. C., Day J. M. D., Tait K. T., Ash R. D., Holdsworth D. W. and Moser D. E. (2014) Characterization of weathering and heterogeneous mineral phase distribution in Brachinites Northwest Africa 4872. *Meteorit. Planet. Sci.* **49**, 1141–1156.
- Le Corre L., Reddy V., Sanchez J. A., Dunn T., Cloutis E. A., Izawa M. R. M., Mann P. and Nathues A. (2015) Exploring exogenic sources for the olivine on Asteroid (4) Vesta. *Icarus* **258**, 483–499.
- Lodders K. (2003) Solar system abundances and condensation temperatures of the elements. *Astrophys J* **591**, 1220–1247.
- Lorand J.-P. and Luguet A. (2016) Chalcophile and siderophile elements in mantle rocks: trace elements controlled by trace minerals. *Rev. Mineral. Geochem.* **81**, 441–488.
- Lorand J.-P., Delpech G., Grégoire M., Moine B., O'Reilly S. Y. and Cottin J.-Y. (2004) Platinum-group elements and the multistage metasomatic history of Kerguelen lithospheric mantle (South Indian Ocean). *Chem. Geol.* **208**, 195–215.
- Kullerud G. and Yoder, Jr., H. S. (1963) Sulfide-silicate reactions. *Carnegie Inst. Washington Yearbook*, 215–218.
- Kullerud G. and Yoder, Jr., H. S. (1964) Sulfide-silicate reactions. *Carnegie Inst. Washington Yearbook*, 218–222.
- Mandler B. E. and Elkins-Tanton L. T. (2013) The origin of eucrites, diogenites, and olivine diogenites: magma ocean crystallization and shallow magma chamber processes on Vesta. *Meteorit. Planet. Sci.* **48**, 2333–2349.
- McCord T. B., Adams J. B. and Johnson T. V. (1970) Asteroid Vesta: spectral reflectively and compositional implications. *Science* **168**, 1445–1447.
- McSween H. Y., Mittlefehldt D. W., Beck A. W., Mayne R. G. and McCoy T. J. (2011) HED meteorites and their relationship to the geology of Vesta and the Dawn Mission. *Space Sci. Rev.* **163**, 141–174.
- McSween H., Ammannito E., Reddy V., Prettyman T., Beck A., De Sanctis M., Nathues A., Le Corre L., O'Brien D., Yamashita N., McCoy T., Mittlefehldt D., Toplis M., Schenk P., Palomba E., Turrini D., Tosi F., Zambon F., Longobardo A., Capaccioni F., Raymond C. and Russell C. (2013) Composition of the Rheasilviabasin, a window into Vesta's interior. *J. Geophys. Res.: Planets* **118**, 335–346.
- Mittlefehldt D. W. (1994) The genesis of diogenites and HED parent body petrogenesis. *Geochim. Cosmochim. Acta* **58**, 1537–1552.
- Mittlefehldt D. W. (2015) Asteroid (4) Vesta: I. The howardite-eucrite-diogenite (HED) clan of meteorites. *Chem. Erde* **75**, 155–183.
- Mittlefehldt D. W., McCoy T. J., Goodrich C. A. and Kracher A. (1998) Non-chondritic meteorites from asteroids. In *Planetary Materials*, vol. 36 (ed. J. J. Papike). Mineralogical Society of America, Washington, pp. 4–1–195.
- Mittlefehldt D. W., Beck A. W., Lee C.-T. A., McSween H. Y. and Buchanan P. C. (2012) Compositional constraints on the genesis of diogenites. *Meteorit. Planet. Sci.* **47**, 72–98.
- Miyahara M., Ohtani E., Yamaguchi A., Ozawa S., Sakai T. and Hirao N. (2014) Discovery of coesite and stishovite in eucrite. *Proc. Natl. Acad. Sci. United States of America* **111**, 10939–10942.
- Nathues A., Hoffmann M., Schäfer M., Thangjam G., Le Corre L., Reddy V., Christensen U., Mengel K., Sierks H., Vincent J., Cloutis E. A., Russell C. T., Schäfer T., Gutierrez-Marques P., Hall I., Ripken J. and Büttner I. (2015) Exogenic olivine on Vesta from Dawn Framing Camera color data. *Icarus* **258**, 467–482.
- Norman M. D. (1981) Petrology of suevite lunar breccia 67016. In *Proceedings of the 12th Lunar and Planetary Science Conference 12B*, pp. 235–252.
- Norman M. D., Keil K., Griffin W. L. and Ryan C. G. (1995) Fragments of ancient lunar crust: petrology and geochemistry of ferroan noritic anorthosites from the Descartes region of the Moon. *Geochim. Cosmochim. Acta* **59**, 831–847.
- Onuma N., Higuchi H., Wakita H. and Nagasawa H. (1968) Trace element partition between 2 pyroxenes and host lava. *Earth Planet. Sci. Lett.* **5**, 47–51.
- Palomba E., Longobardo A., De Sanctis M. C., Zinzi A., Ammannito E., Marchi S., Tosi F., Zambon F., Capria M. T., Russell C. T., Raymond C. A. and Cloutis E. A. (2015) Detection of new olivine-rich locations on Vesta. *Icarus* **258**, 120–134.
- Pang R. L., Zhang A. C., Wang S. Z., Wang R. C. and Yurimoto H. (2016) High-pressure minerals in eucrite suggest a small source crater on Vesta. *Sci. Rep.* **6**, 26063.
- Papike J. J., Karner J. M. and Shearer C. K. (2003) Determination of planetary basalt parentage: a simple technique using the electron microprobe. *Am. Miner.* **88**, 469–472.
- Patzer A. and McSween H. Y. (2012) Ordinary (mesostasis) and not-so-ordinary (symplectites) late-stage assemblages in howardites. *Meteorit. Planet. Sci.* **47**, 1475–1490.
- Peslier A. H., Brandon A. D., Tarduno J. A. and Mittlefehldt D. W. (2015) Petrology of diogenite NWA 5480, a pristine olivine-rich deformed harzburgite. In *46th Lunar and Planetary Science Conference, Abstract #2221*.
- Petaev M. I., Barsukova L. D., Lipschutz M. E., Wang M. S., Ariskin A. A., Clayton R. N. and Mayeda T. K. (1994) The Divnoe meteorite: petrology, chemistry, oxygen isotopes and origin. *Meteoritics* **29**, 182–199.
- Righter K. and Drake M. J. (1997) A magma ocean on Vesta: core formation and petrogenesis of eucrites and diogenites. *Meteorit. Planet. Sci.* **32**, 929–944.
- Roedder E. and Weiblen P. W. (1974) Petrology of clasts in lunar breccia 67915. In *Proceedings of the Fifth Lunar Conference*, pp. 303–318.
- Russell C. T., Raymond C. A., Coradini A., McSween H. Y., Zuber M. T., Nathues A., De Sanctis M. C., Jaumann R., Konopliv A. S., Preusker F., Asmar S. W., Park R. S., Gaskell R., Keller H. U., Mottola S., Roatsch T., Scully J. E. C., Smith D. E., Tricarico P., Toplis M. J., Christensen U. R., Feldman W. C., Lawrence D. J., McCoy T. J., Prettyman T. H., Reedy R. C., Sykes M. E. and Titus T. N. (2012) Dawn at Vesta: testing the protoplanetary paradigm. *Science* **33**, 684–686.

- Ruzicka A., Snyder G. A. and Taylor L. A. (1997) Vesta as the howardite, eucrite and diogenite parent body: implications for the size of a core and for large-scale differentiation. *Meteorit. Planet. Sci.* **32**, 825–840.
- Ruzicka A., Grossman J., Bouvier A., Herd C. D. K. and Agee C. B. (2014) *The Meteoritical bulletin, No. 102*. The Meteoritical Society, p. 248.
- Sack R. O. and Ghiorso M. S. (1989) Importance of considerations of mixing properties in establishing an internally consistent database: thermochemistry of minerals in the system  $Mg_2SiO_4$ - $Fe_2SiO_4$ - $SiO_2$ . *Contrib. Miner. Petrol.* **102**, 41–68.
- Sack R. O. and Ghiorso M. S. (1994a) Thermodynamics of multicomponent pyroxenes: I. Formulation of a general model. *Contrib. Miner. Petrol.* **116**, 277–286.
- Sack R. O. and Ghiorso M. S. (1994b) Thermodynamics of multicomponent pyroxenes: II. Phase relations in the quadrilateral. *Contrib. Miner. Petrol.* **116**, 287–300.
- Sack R. O. and Ghiorso M. S. (1994c) Thermodynamics of multicomponent pyroxenes: III. Calibration of  $Fe^{2+}(Mg)^{-1}$ ,  $TiAl(MgSi)^{-1}$ ,  $TiFe^{3+}(MgSi)^{-1}$ ,  $AlFe^{3+}(MgSi)^{-1}$ ,  $NaAl(CaMg)^{-1}$ ,  $Al_2(MgSi)^{-1}$  and  $Ca(Mg)^{-1}$  exchange reactions between pyroxenes and silicate melts. *Contrib. Miner. Petrol.* **118**, 271–296.
- Sack R. O. and Ghiorso M. S. (1991a) An internally consistent model for the thermodynamic properties of Fe-Mg-titanomagnetite-aluminate spinels. *Contrib. Miner. Petrol.* **106**, 474–505.
- Sack R. O. and Ghiorso M. S. (1991b) Chromian spinels as petrogenetic indicators: thermodynamics and petrological applications. *Am. Miner.* **76**, 827–847.
- Sack R. O., Azeredo W. J. and Lipschutz M. E. (1991) Olivine diogenites: the mantle of the eucrite parent body. *Geochim. Cosmochim. Acta* **55**, 1111–1120.
- Shearer C. K., Burger P. V., Guan Y., Papike J. J., Sutton S. R. and Atudorei N.-V. (2012) Origin of sulfide replacement textures in lunar breccias. Implications for vapor element transport in the lunar crust. *Geochim. Cosmochim. Acta* **83**, 138–158.
- Stolper E. (1977) Experimental petrology of eucrite meteorites. *Geochim. Cosmochim. Acta* **41**, 587–611.
- Toulmin P. and Barton P. B. (1964) A thermodynamic study of pyrite and pyrrhotite. *Geochim. Cosmochim. Acta* **28**, 641–671.
- Treiman A. H., Lanzirotti A. and Xirouchakis D. (2004) Ancient water on asteroid 4 Vesta: evidence from a quartz veinlet in the Serra de Magé eucrite meteorite. *Earth Planet. Sci. Lett.* **219**, 189–199.
- Turrini D., Svetsov V., Consolmagno G., Sirono S. and Pirani S. (2016) Olivine on Vesta as exogenous contaminants brought by impact: constraints from modeling Vesta's collisional history and from impact simulations. *Icarus* **280**, 328–339.
- Wang W. Y. and Yurimoto H. (1993) Analysis of rare earth elements in garnet by SIMS. *Ann. Rep. Inst. Geosci. Univ. Tsukuba* **19**, 87–91.
- Warren P. H., Rubin A. E., Isa J., Gessler N., Ahn I. and Choi Bye.-Gak. (2014) Northwest Africa 5738: multistage fluid-driven secondary alteration in an extraordinary evolved eucrite. *Geochim. Cosmochim. Acta* **141**, 199–227.
- Yamaguchi A., Barrat J. A., Ito M. and Bohn M. (2011) Posteucretic magmatism on Vesta: evidence from the petrology and thermal history of diogenites. *J. Geophys. Res.* **116**, E08009. <https://doi.org/10.1029/2010JE003753>.
- Yurimoto H., Yamashita A., Nishida N. and Sueno S. (1989) Quantitative SIMS analysis of GSJ rock reference samples. *Geochem. J.* **23**, 215–236.
- Zhang A. C., Itoh S., Sakamoto N., Wang R. C. and Yurimoto H. (2014) Origins of Al-rich chondrules: clues from a compound Al-rich chondrule in the Dar al Gani 978 carbonaceous chondrite. *Geochim. Cosmochim. Acta* **130**, 78–92.
- Zhang A. C., Wang R. C., Hsu W. B. and Bartoschewitz R. (2013) Record of S-rich vapors on asteroid 4 Vesta: sulfurization in the Northwest Africa 2339 eucrite. *Geochim. Cosmochim. Acta* **109**, 1–13.
- Zhang Y. X. (2010) Diffusion in minerals and melts: theoretical background. *Rev. Mineral. Geochem.* **72**, 5–59.

Associate editor: James M.D. Day